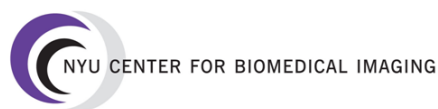


# **Sodium Magnetic Resonance Imaging: Biomedical Applications \***

Guillaume Madelin

New York University Langone Medical Center  
Department of Radiology - Center for Biomedical Imaging  
New York, NY 10016, USA



December 21, 2012

\*This article is a long version of a review article that will be published in Journal of Magnetic Resonance Imaging in 2013.



## Abstract

In this article, we present an up-to-date overview of the potential biomedical applications of sodium MRI *in vivo*. Sodium MRI is a subject of increasing interest in translational research as it can give some direct and quantitative biochemical information on the tissue viability, cell integrity and function, and therefore not only help the diagnosis but also the prognosis of diseases and treatment outcomes. It has already been applied *in vivo* in most of human tissues, such as brain for stroke or tumor detection and therapeutic response, in breast cancer, in articular cartilage, in muscle and in kidney, and it was shown in some studies that it could provide very useful new information not available through standard proton MRI. However, this technique is still very challenging due to the low detectable sodium signal in biological tissue with MRI and hardware/software limitations of the clinical scanners. The article is divided in three parts: (1) the role of sodium in biological tissues, (2) a short review on sodium magnetic resonance, and (3) a review of some studies on sodium MRI on different organs/diseases to date.





# Contents

<b>Introduction</b>	<b>7</b>
<b>1 Sodium in Biological Tissues</b>	<b>9</b>
1.1 Homeostasis . . . . .	9
1.2 $\text{Na}^+/\text{K}^+$ -ATPase . . . . .	9
<b>2 Sodium Nuclear Magnetic Resonance</b>	<b>11</b>
2.1 Short History of Sodium NMR . . . . .	11
2.2 Sodium NMR Properties . . . . .	12
2.3 Tensors and Hamiltonians . . . . .	12
2.4 Quadrupolar Relaxation and NMR Spectra . . . . .	15
2.5 Spectra Models . . . . .	18
2.6 Multiple Quantum Filters (MQF) . . . . .	19
2.7 Fluid and Extracellular Sodium Suppression . . . . .	20
2.8 RF Pulse Sequences . . . . .	22
2.9 Sodium Quantification . . . . .	23
2.10 Limitations and Prospects . . . . .	23
<b>3 Biomedical Applications</b>	<b>25</b>
3.1 Brain . . . . .	25
3.2 Breast . . . . .	32
3.3 Heart . . . . .	33
3.4 Muscle . . . . .	34
3.5 Cartilage . . . . .	37
3.6 Abdomen . . . . .	39
3.7 Whole Body . . . . .	42
3.8 Cancer and Chemotherapeutic Response . . . . .	42
<b>Conclusion</b>	<b>47</b>
<b>Bibliography</b>	<b>48</b>



# Introduction

Proton magnetic resonance imaging (MRI) can generate more than 30 different kinds of image contrast (and still counting) which can give the physicians crucial information of the anatomy, and sometimes function, of the organs under investigation. All organs and most of the known diseases (if not all) can be studied with this imaging technique in order to assess their presence and/or degree of possible harm to the body. However very often, the information from standard MRI cannot provide direct biochemical information about the health of the tissues, such as cell integrity and tissue viability, or predict possible outcomes from different treatments. Sodium MRI could provide some of this complementary information in a quantitative and non-invasive manner.

Sodium, symbol  $^{23}\text{Na}$ , is a quadrupolar nucleus with spin  $3/2$  which yields the second strongest nuclear magnetic resonance (NMR) signal among all nuclei present in biological tissues, after proton  $^1\text{H}$ . The NMR sensitivity for sodium is 9.2% of the proton sensitivity and the concentration *in vivo* is approximately 2000 times lower than the water proton concentration. As a consequence, sodium MRI have a average signal-to-noise (SNR) ratio which is around 3000 to 20000 times lower than the proton MRI SNR (depending on organs). Due to the increase of the available magnetic fields for MRI scanners (1.5T, 3T, 7T, 9.4T), hardware capabilities such as high gradient strengths with high slew rates, and new double-tuned radiofrequency (RF) coils, sodium MRI is now possible in a reasonable time (around 10 to 15 minutes) with a resolution of a few millimeters and has already been applied *in vivo* in many human organs such as human brain for tumor and stroke, cartilage, kidneys, heart, muscle or breast cancer, that will be described in this review article. Sodium MRI is still a subject of investigation for assessing its medical utility as a complement to proton MRI or other imaging modalities such as PET and CT, and determine the new functional/biochemical that it can provide.

The goal of this review is to describe some potential biomedical applications of sodium MRI *in vivo* and is divided in three parts:

1. The role of sodium in biological tissues.
2. A short review on sodium magnetic resonance physics.
3. An overview of some studies on sodium MRI on different organs/diseases to date.



# 1 Sodium in Biological Tissues

## 1.1 Homeostasis

Sodium is a vital component of the human body. It is an important electrolyte that helps maintain the homeostasis of the organism through osmoregulation (maintain blood and body fluid volume) and pH regulation [1]. It is also involved in the cell physiology through the transmembrane electrochemical gradient, in heart activity, in the transmission of nerve impulses and muscle contractions through propagation of action potential in neurons and muscle cells via the sodium channels. Sodium concentrations are therefore very sensitive to changes in metabolic state of tissues and integrity of cell membranes. The intracellular volume fraction is around 80% of the tissues with a sodium concentration of 10-15 mM (or mmol/L), and the extracellular volume fraction (including the vascular compartment) is around 20%, with a sodium concentration of 140-150 mM. Cells in healthy tissues maintain this large sodium concentration gradient between the intracellular and extracellular compartments across the cell membrane, and any impairment of energy metabolism or insult to the cell membrane integrity leads to an increase on intracellular sodium concentration. The sodium influx and efflux in cells can occur by several routes such as  $\text{Na}^+$  channels,  $\text{Na}^+/\text{Ca}^{2+}$  exchange (NCX),  $\text{Na}^+/\text{H}^+$  exchange (NHE),  $\text{Na}^+/\text{bicarbonate}$  ( $\text{HCO}_3^-$ ) cotransporter,  $\text{Na}^+/\text{K}^+ / 2\text{Cl}^-$  cotransporter,  $\text{Na}^+/\text{Mg}^{2+}$  exchange and most importantly through the  $\text{Na}^+/\text{K}^+$ -ATPase [2].

## 1.2 $\text{Na}^+/\text{K}^+$ -ATPase

The  $\text{Na}^+/\text{K}^+$ -ATPase (also called sodium-potassium pump, or just sodium pump) is present within the membrane of every animal cell [3, 4]. It is a plasma membrane-associated protein complex that is expressed in most eukaryotic cells and can be considered either as an enzyme (ATPase) or as an ion transporter (the  $\text{Na}^+$ -pump). Its main function is to maintain the sodium and potassium gradients across the membrane, and therefore participates in the resting potential of the cell, by pumping three intracellular sodium ions out of the cell and two extracellular potassium ions within the cell (see Fig. 1.2.1).

## 1 Sodium in Biological Tissues

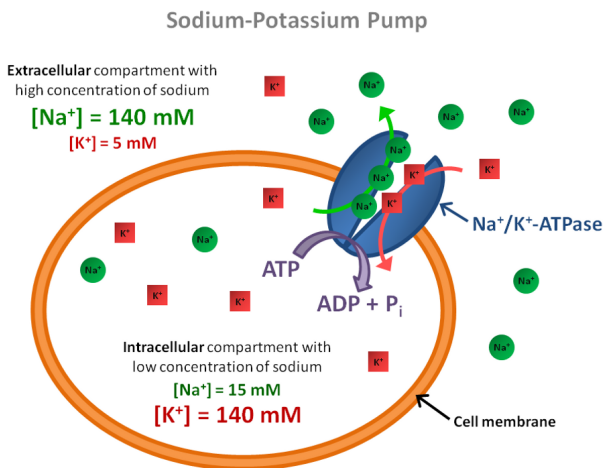


**Figure 1.2.1:** Schematics of the sodium-potassium pump ( $Na^+/K^+-ATPase$ ).

This ion transport is performed against the electrochemical  $Na^+$  and  $K^+$  gradients existing across the cell membrane and therefore requires energy provided by adenosine triphosphate (ATP) hydrolysis. This high electrochemical gradient is essential to protect the cell from bursting as a result of osmotic swelling and also creates a potential that is used for transmitting nerve impulses and for pumping ions (such as protons, calcium, chloride, and phosphate) and metabolites and nutrients across the cell membrane (such as glucose and amino acids) or neurotransmitters (such as glutamate in astrocyte cells). ATPase activity and ion transport are intimately linked and are two aspects of the same function. Regulation of  $Na^+/K^+-ATPase$  therefore plays a key role in the etiology of some pathological processes. For example, when the de-

mand for ATP exceeds its production, the ATP supply for the  $Na^+/K^+-ATPase$  will be insufficient to maintain the low intracellular sodium concentration and thus an increase of intracellular sodium concentration can be observed.

## 2 Sodium Nuclear Magnetic Resonance

### 2.1 Short History of Sodium NMR

The bar chart in Fig. 2.1.1 presents the distribution of publications on sodium NMR and MRI over the years since the discovery of magnetic resonance in the 1940s [5, 6]. Data was obtained from a research in Google Scholar with the research key words “sodium” or “ $^{23}\text{Na}$ ” along with “magnetic resonance” or “magnetic resonance imaging” or “MRI” or “NMR” in the publication title.

It is interesting to notice the peak of publications in the period 1991-1995 for the combination of sodium NMR (spectroscopy) and MRI, which then decreases while the publications on sodium MRI alone continues to increase since the early 1980s. A shift of interest appears from sodium NMR spectroscopy to MRI, which is probably due to the recent availability of scanners with high fields and therefore the possibility of performing sodium MRI *in vivo* in reasonable times, opening to new exciting research perspectives.

Briefly, biological tissues were already investigated with sodium NMR spectroscopy in the early 1970s [7, 8] and with sodium MRI in the early 1980s [9–11], first on animals *in vivo* and then on human brain [12] and human heart and abdomen [13]. Sodium MRI was therefore applied for brain tumor and ischemia detection in the late 1980s [14]. The years 1990s will see an increase of interest in sodium MRI, due to the increase of the magnetic fields in scanners, improvements of electronics and RF coils, and new rapid sequences that allow to acquire sodium images in a few minutes with a reasonable resolution of a few millimeters [15], or new contrasts such as triple quantum filtered images [16–18]. This trend continued in the 2000s until today.

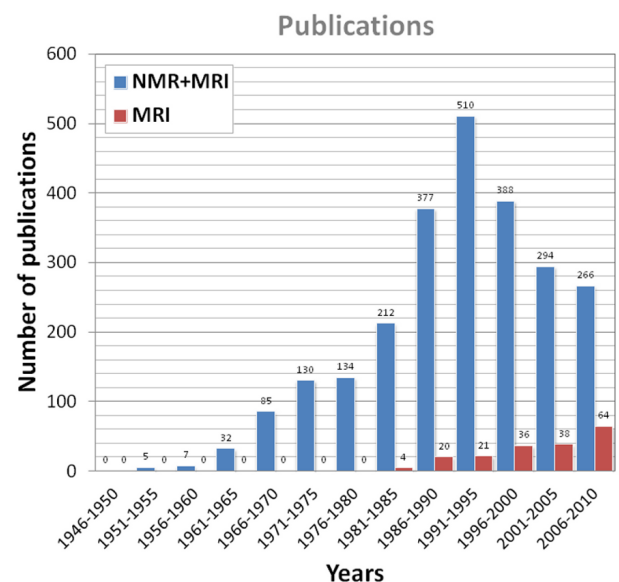


**Figure 2.1.1:** Publication statistics on sodium NMR and MRI. Data was obtained from a research in Google Scholar with the research key words “sodium” or “ $^{23}\text{Na}$ ” along with “magnetic resonance” or “magnetic resonance imaging” or “MRI” or “NMR” in the publication title.

## 2.2 Sodium NMR Properties

The sodium nucleus has a spin  $I = 3/2$  and possesses a quadrupolar moment  $Q$  which interacts with the electric field gradients (EFG) generated by the electronic distribution around the nucleus. In general, sodium in solids experience quadrupolar interactions while in liquids, the static quadrupolar interaction is averaged to zero. In the intermediate regimes, e.g. in biological tissues, the quadrupolar interaction results in a biexponential relaxation behavior. The dominance of quadrupolar relaxation mechanism for NMR signals can allow a sensitive characterization of the molecular environment of the sodium ions. A short  $T_2$  component  $T_{2\text{short}} = 0.5\text{-}5$  ms generally contributes to 60% of the signal in living tissue and a long component  $T_{2\text{long}} = 15\text{-}30$  ms corresponds to 40% of the signal. In order to detect both  $T_2$  components, imaging techniques with ultrashort echo time (UTE) of less than 0.5 ms are required. But it is difficult to obtain reliable information about the biexponential relaxation from these conventional simple single-pulse / single quantum (SQ) NMR methods. It has been shown that in the presence of biexponential relaxation, multiple quantum coherences (MQC) can be created and detected with MQF sequences [19], and thus give information about the interaction of sodium ions with their environment. Ranges of sodium concentrations and relaxation times in some human tissues *in vivo* are given in Table 2.1

**Table 2.1:** Range of sodium concentrations and relaxation times in some human tissues *in vivo*.

Tissue		[Na <sup>+</sup> ] (mM)	T1 (ms)	T2 <sub>short</sub> (ms)	T2 <sub>long</sub> (ms)
Brain	WM	20-60	15-35	0.8-3	15-30
	GM	30-70	15-35	0.8-3	15-30
	CSF	140-150	50-55	-	55-65
Cartilage		250-350	15-25	0.5-2.5	10-30
Blood		140-150	20-40	2-3	12-20
Muscle		15-30	12-25	1.5-2.5	15-30

## 2.3 Tensors and Hamiltonians

### Irreducible Spherical Tensor Operator (ISTO)

A convenient way to describe the various processes occurring during the pulse sequence is by the irreducible spherical tensor operator (ISTO) basis [20–22],  $T_{nm}$ , where  $n$  is the rank and  $m$  is the order (or coherence) of the tensor with  $|m| < n$ . These tensors are composed of combinations of the more familiar spin operators  $I_z$  and  $I_{\pm} = I_x \pm iI_y$ . The ISTO used to describe the density operator and the Hamiltonians for a spin  $3/2$  are given in Table 2.2. In order to follow the sequence of events at high magnetic fields, one should bear in mind two simple rules:



1. A non-selective radiofrequency (RF) pulse can change the coherence  $m$  within the limits of  $|m| < n$ .
2. Changes in the rank  $n$  can occur by relaxation and modulation by quadrupolar, dipolar or J-coupling, keeping the same value of  $m$ .

In the following sections, we consider that the spin system evolves only under the influence of Zeeman, quadrupolar and RF Hamiltonians [22, 23].

**Table 2.2:** Irreducible spherical tensor operators (ISTO) for spin  $I = 3/2$ .

ISTO	Value	Definition
$T_{00}$	1	Identity
$T_{10}$	$I_z$	Longitudinal magnetization
$T_{1\pm 1}$	$\mp \frac{1}{\sqrt{2}} I_{\pm}$	Rank 1 SQC
$T_{20}$	$\frac{1}{\sqrt{6}} (3I_z^2 - I(I+1))$	Quadrupolar magnetization
$T_{2\pm 1}$	$\mp \frac{1}{2} [I_z, I_{\pm}]_+$	Rank 2 SQC
$T_{2\pm 2}$	$\frac{1}{2} I_{\pm}^2$	Rank 2 DQC
$T_{30}$	$\frac{1}{\sqrt{10}} (5I_z^3 - (3I(I+1) - 1) I_z)$	Octopolar magnetization
$T_{3\pm 1}$	$\mp \frac{1}{4} \sqrt{\frac{3}{10}} [5I_z^3 - I(I+1) - \frac{1}{2}, I_{\pm}]_+$	Rank 3 SQC
$T_{3\pm 2}$	$\frac{\sqrt{3}}{4} [I_z, I_{\pm}^2]_+$	Rank 3 DQC
$T_{3\pm 3}$	$\mp \frac{1}{2\sqrt{2}} I_{\pm}^3$	Rank 3 TQC

SQC, DQC and TQC are respectively the single, double and triple quantum coherences.

The anticommutator for the operators A and B is defined as  $[A, B]_+ = AB + BA$ .

### Zeeman Hamiltonian ( $H_z$ )

The Zeeman Hamiltonian is given by

$$H_z = \omega_0 T_{10}, \quad (2.3.1)$$

with  $\omega_0 = \gamma_{Na} B_0$  the Larmor angular frequency,  $\gamma_{Na} = 70.808493 \times 10^6 \text{ rad} \cdot \text{T}^{-1} \cdot \text{s}^{-1}$  the sodium gyromagnetic ratio (26% of the proton  $\gamma_p$ ) and  $B_0$  the magnetic field.

All the following Hamiltonians are expressed in the Larmor frequency rotating frame, in which this  $H_z$  vanishes.

### Quadrupolar Hamiltonian ( $H_Q$ )

#### Electric field gradient (EFG)

The nuclear quadrupole interaction is determined by the orientation, magnitude and temporal duration of EFG generated by the electronic configuration of the molecular environment surrounding the nucleus. If  $V(x, y, z)$  is the electrostatic potential produced by electrons at the point  $(x, y, z)$ , EFG can be described by the tensor  $V_{\alpha\beta}$  with the components:

$$V_{\alpha\beta} = \frac{\partial^2 V}{\partial \alpha \partial \beta}, \quad (\text{with } \alpha, \beta = x, y, z). \quad (2.3.2)$$

If we choose the principal axes of the symmetric tensor  $V_{\alpha\beta}$  as coordinates axes, the cross-terms vanish, i.e.  $V_{xy} = V_{xz} = V_{yz} = 0$ . It is common to label the remaining components such that  $|V_{zz}| \geq |V_{yy}| \geq |V_{xx}|$ , and to define  $V_{zz} = eq$  ( $e$  is the unit electric charge) and the anisotropy parameter:

$$\eta = \frac{V_{xx} - V_{yy}}{V_{zz}}, \quad 0 \leq \eta \leq 1. \quad (2.3.3)$$

#### Quadrupolar Hamiltonian

The quadrupolar interaction of the  $^{23}\text{Na}$  spin with the EFG is represented by the quadrupolar Hamiltonian  $H_Q$ . In the principal axis system (PAS) of  $V_{\alpha\beta}$ , it reads:

$$H_Q = \omega_Q \sum_{m=-2}^2 (-1)^m F_{2,-m} T_{2m}, \quad (2.3.4)$$

with the PAS spatial tensor components:

$$\begin{aligned} F_{2,0} &= \sqrt{\frac{3}{2}}, \\ F_{2,\pm 1} &= 0, \\ F_{2,\pm 2} &= \frac{\eta}{2}, \end{aligned} \quad (2.3.5)$$

and the quadrupolar angular frequency:

$$\omega_Q = \frac{e^2 q Q}{6\hbar}. \quad (2.3.6)$$

#### Radiofrequency Hamiltonian ( $H_{RF}$ )

If the RF pulse is applied on-resonance along the  $x$ -axis with field strength  $\omega_{RF}(t) = \gamma_{Na} B_1(t)$ , with  $B_1(t)$  the RF magnetic field, the corresponding RF Hamiltonian is time-dependent and

reads:

$$H_{RF} = \omega_{RF} I_x = \omega_{RF} \frac{1}{\sqrt{2}} (T_{1-1} - T_{1+1}). \quad (2.3.7)$$

### Total Hamiltonian ( $H$ )

In the Larmor rotating frame, the total Hamiltonian is then:

$$H = H_{RF} + H_Q. \quad (2.3.8)$$

## 2.4 Quadrupolar Relaxation and NMR Spectra

Depending on the motional regime of the system, the energy levels of the system and the relaxation rates can be modified, giving one or many NMR peaks in the one-pulse single quantum (SQ)  $^{23}\text{Na}$  spectra, as shown on Fig. 2.4.1 [24]. The following three motional regimes and four different types of spectra are possible, depending on the nature of the spin dynamics and the nature of the molecular environment [24–27]. In the following section, we consider that the  $\text{Na}^+$  ions are present in a single compartment with a single rotational correlation time  $\tau_c$ . We also consider that the system is in the Redfield regime, where the relaxation of spin  $3/2$  is described by second-order perturbation theory, and where the spin dynamics can be solved analytically [22].

### Isotropic Motion With Motional Narrowing ( $\omega_0 \tau_c \ll 1$ )

In a system of rapid motion such as a fluid, all orientations of the EFG are equally probable. In this isotropic system, the quadrupolar interaction is averaged to zero on the time scale of  $2\pi/\omega_0$  and the four energy levels of the spin  $3/2$  are equally distant by the angular frequency  $\omega_0$ . The  $^{23}\text{Na}$  spectrum is then composed of a single resonance line at  $\omega_0$ , as shown in the type-d spectrum in Fig. 2.4.1. Both transverse and longitudinal relaxations are simple exponential decays. The liquid-like type-d spectrum was obtained from NaCl in aqueous solution.

### Isotropic Motion Without Motional Narrowing ( $\omega_0 \tau_c \sim 1$ )

In tissues where the macromolecular motion associated with the nucleus is isotropic but of the same order of the Larmor frequency, the quadrupolar interaction dominates the relaxation. The satellite and central transitions have different transverse relaxation rates  $R_1^{(\pm 1)}$  and  $R_2^{(\pm 1)}$  respectively, and are dynamically shifted from the Larmor frequency with shifts  $K_1$  and  $K_2 - K_1$ , respectively. However, these shifts are much smaller than the linewidths and very difficult to detect. This situation can correspond to a biological-like type-c spectrum in Fig. 2.4.1, which was

## Energy Levels and Spectra

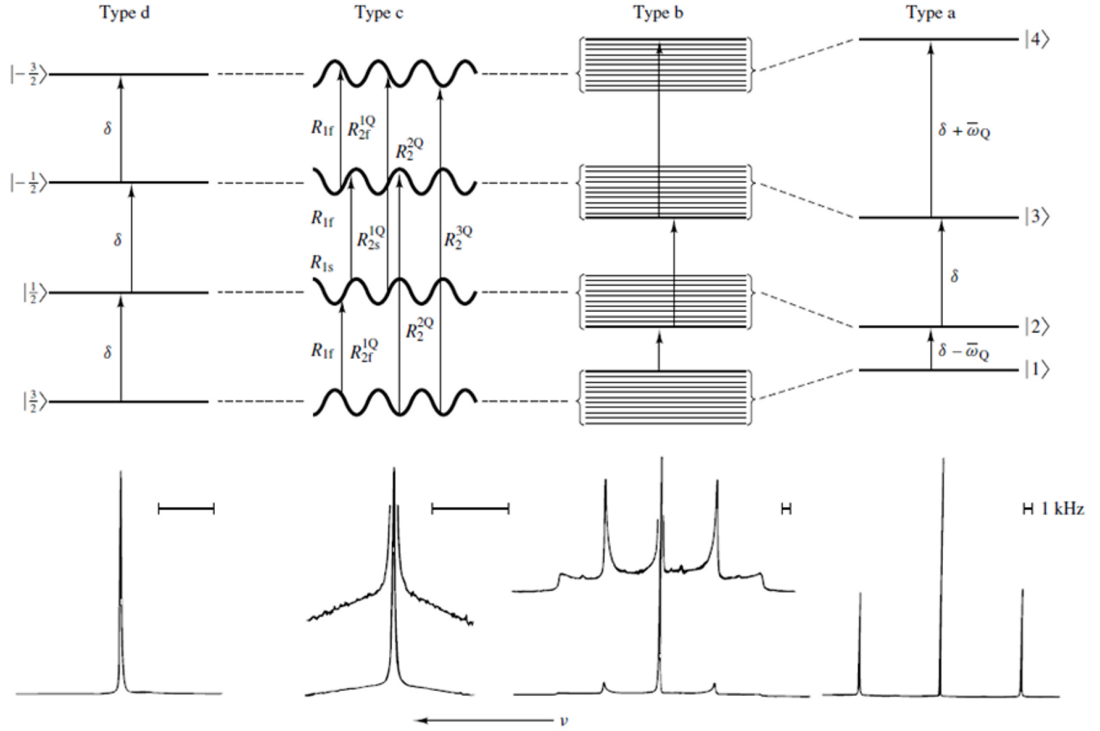


**Figure 2.4.1:** Typical energy levels and corresponding NMR spectra of sodium nuclei in different environments. Four types of motionally narrowed SQ spectra are possible (a, b, c, and d). The **type-a** (crystal-like) and **type-b** (powder-like) spectra are of Na<sup>+</sup> in aqueous suspensions of oriented and unoriented dodecyl sulfate micelles, respectively. The **type-c** (homogeneous, biexponential, super-Lorentzian-like) spectrum is that of Na<sup>+</sup> in an aqueous solution that has a high concentration of micelle-solubilized gramicidin channels. The **type-d** (liquid-like) spectrum is that of NaCl in H<sub>2</sub>O. From Rooney W. et al. NMR in Biomedicine 4, 209-226, 1991. Reproduced by permission of Wiley-Blackwell.

obtained from solubilized micelles in an aqueous solution. It is a “homogeneous” (“biexponential”, “super-Lorentzian”) spectrum, in which the satellite peaks have essentially coalesced into a single, broad, homogeneous peak. The relaxation rates are:

$$\begin{aligned} R_1^{(\pm 1)} &= J_0 + J_1 \pm iK_1, \\ R_2^{(\pm 1)} &= J_1 + J_2 \mp i(K_1 - K_2) \end{aligned} \quad (2.4.1)$$

with the spectral densities (with  $m = 0, 1, 2$ ):

$$\begin{aligned} J_m(m\omega) &= \frac{(2\pi)^2}{20} \left( \frac{\chi^2 \tau_c}{1 + (m\omega)^2 \tau_c^2} \right), \\ K_m(m\omega) &= \omega \tau_c J_m(m\omega). \end{aligned} \quad (2.4.2)$$

The spectral densities  $J_m$  and  $K_m$  are the real and imaginary parts of the FFT of the EFG correlation function and  $\chi$  is the root mean square coupling constant. Even in the absence of any quadrupolar splitting, biexponential relaxation can create MQC which can be detected by triple quantum filtering (TQF).

### Anisotropic Motion ( $\omega_0\tau_c > 1$ )

The sodium nuclei experiment non-averaged EFG and therefore a residual quadrupolar interaction (RQI). The SQ relaxation rates are:

$$\begin{aligned} R_1^{(1)} &= J_0 + J_1 + J_2 - \sqrt{J_2^2 - \omega_Q^2}, \\ R_2^{(1)} &= J_1 + J_2, \\ R_3^{(1)} &= J_0 + J_1 + J_2 + \sqrt{J_2^2 - \omega_Q^2}. \end{aligned} \quad (2.4.3)$$

Depending on the magnitude of  $J_2$ , three situations can occur:

1. If  $\omega_Q < J_2$ , the relaxation rates are real and there is no line splitting despite the presence of RQI. The SQ spectrum is a sum of three Lorentzians. The RQI influences the linewidths and amplitudes of the components, there is a very small splitting in the spectrum, but it is masked by the larger SQ linewidths. This case can be still described by a type-c spectrum in Fig. 2.4.1. In this case, the Double Quantum filter (DQF) signal due to even rank coherence  $T_{2\pm 2}$  can be used to detect and measure  $\omega_Q$ .
2. If  $\omega_Q > J_2$ , the relaxation eigenvalues and corresponding to outer transitions are complex and the satellite transitions are shifted by  $\pm\sqrt{\omega_Q^2 - J_2^2}$  from the central line. This case corresponds to a powder-like type-b spectrum in Fig. 2.4.1, which was acquired from unoriented micelles in aqueous solution (unoriented liquid crystal). The DQF signal from  $T_{2\pm 2}$  can also be used to measure  $\omega_Q$ .
3. If  $\omega_Q \gg J_2$ , the energy levels are all shifted by the RQI resulting in three distinct peaks in the spectrum. The central transition and the two satellite transitions are separated by  $\omega_Q$ . This frequency separation between the lines provides therefore indirect information about RQI and the magnitude of ordering in the system. This case can be described by a crystal-like type-a spectrum in Fig. 2.4.1, which was obtained from oriented micelles in aqueous solution (oriented liquid crystal). Relative areas of the peaks are 3:4:3.

## 2.5 Spectra Models

In tissue,  $\text{Na}^+$  aquo cations exist in compartmentalized spaces (intra- and extracellular compartments for example) and encounter an abundance of charged macromolecules. The nature of tissue is such that most of the sodium spectra are likely to be of type c or type b, or intermediate or superpositions of these. Several models were therefore developed in order to understand the SQ sodium spectra in biological tissues and are described in more details in Ref. [24, 26, 28] and references herein.

### Debye Model (DM)

The DM is the simplest model for the quadrupolar relaxation mechanism and is based on the assumption that the random fluctuation of the EFG tensor strength and orientation that can be described with a single correlation time,  $\tau_c$ . This is the model that was used to describe the spectra in the previous section (quadrupolar relaxation), assuming that the sodium ions are all in a single environmental compartment and that no exchange between compartments occurs. However, this model is too simple to describe sodium spectra in even simple biological tissues such as bovine serum albumin in saline solution or suspensions of yeast cells.

### Discrete Exchange Model (DEM)

The DEM is a more complex model based on equilibrium chemical exchange between distinct sites that have different quadrupolar properties. These individual sites can be each characterized by a Debye model (single  $\tau_c$ ). For example, the James-Noggle exchange occurs between two different type-d sites and can yield only a resultant type-d spectrum. Bull exchange happens between a type-d site and a type-c site and can yield either type of resultant spectrum, depending on the lability of the exchange on the timescale determined by the properties of the two sites. Chan exchange occurs between a type-d site and a type-a site and can produce all kinds of resultant spectra, depending on the lability of the exchange or the random orientation distribution of the type-a sites. However, a two-site DEM model has at least six (or even eight, if temperature is included) independent parameters to describe the resultants spectra, and a three-site exchange model requires at least 13 independent parameters. Analyzing the tissue situation with a realistic DEM is therefore very difficult.

### Berendsen-Edzes Model (BEM)

The BEM seems is a more realistic model which focuses on the EFG tensor projection fluctuations caused by motions of the inner hydration shell of the ion  $\text{Na}^+(\text{aq})$ , that are very powerful and very

rapid. Slower modulations also occur, usually of lower amplitudes, and are generated as the aquo ion diffuses and encounters macromolecules. The BEM mechanism is based on the concept of a sample domain, as experienced by a diffusing aquo ions, which must be at least as large as the average volume sampled by the diffusional excursions during the lifetime of an NMR coherence. The BEM can therefore be useful for describing spectra by modeling domains with the same (type-a) or random (type-b) orientations. A type-c spectrum can also be described using BEM, for  $\text{Na}^+$  in the blood plasma for example, where rapid modulations of the inner hydration sphere domain happen altogether with isotropic slow fluctuations of the EFG by diffusion. But this model is still very difficult to interpret in complex biological tissues.

### Other Models

Some other more complex models such as continuous diffusion models, models with distributions of  $\tau_c$  values, or Debye models with a distribution of  $\omega_Q$  values were also developed in order to describe more accurately sodium spectra in biological tissues.

### Rooney-Springer Protocol

In order to really have a accurate understanding of the sodium NMR data acquisitions in biological tissues, Rooney and Springer [24] proposed a protocol in five steps. Although their complete realization is very difficult, if not impossible, it is still important to consider them and to try to complete at least some of them in order to have a good approximate understanding of the results we obtain from sodium NMR spectroscopy or MRI *in vivo*:

1. Discriminate the SQ resonances from as many physiological compartments as possible.
2. Discriminate the spectral type (a, b, c or d) of each resonance.
3. Determine the numbers of magnetically distinct populations in slow exchange for each resonance (the type of which has been determined above).
4. Measure as many relaxation times values as possible for each population.
5. Interpret the measured relaxation times values.

## 2.6 Multiple Quantum Filters (MQF)

In order to detect MQC from different types of spectrum and therefore obtain some information about the biological environment of the sodium nuclei, MQF can be implemented before the NMR acquisitions [19, 29–31]. MQF are described in Fig. 4. For all MQF experiments, the RF pulses were considered as hard pulses ( $\omega_{RF} \gg \omega_Q$ ).

A first RF pulse of angle  $\theta_1$  and phase  $\phi_1$  is applied to the system to flip the longitudinal magnetization  $T_{10}$  into the transverse plane, giving a transverse magnetization  $T_{1\pm 1}$ . During the preparation time  $\tau$ , the transverse magnetization  $T_{1\pm 1}$  evolves in the presence of relaxation and/or RQI, creating single quantum coherences (SQC) with different rank  $T_{1\pm 1}$ ,  $T_{2\pm 1}$ ,  $T_{3\pm 1}$ .

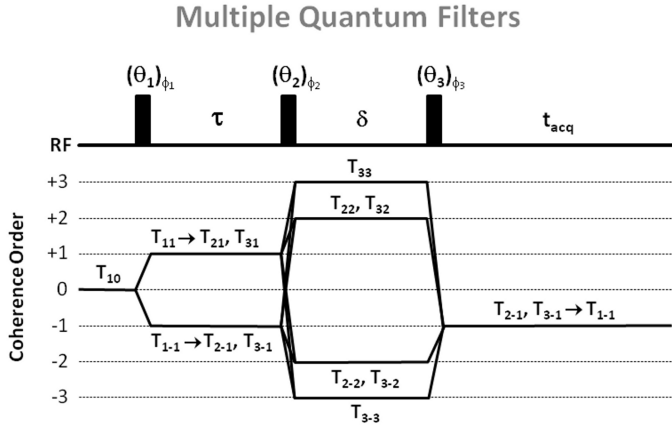


**Figure 2.6.1:** Multiple quantum filters (MQF) and coherence order transfers. For triple quantum filter (TQF) with six-phase cycling,  $\theta_1 = \theta_2 = \theta_3 = 90^\circ$ ,  $\phi_1 = 30^\circ, 90^\circ, 150^\circ, 210^\circ, 270^\circ, 300^\circ$ ,  $\phi_2 = \phi_1 + 90^\circ$ ,  $\phi_3 = 0^\circ$ . For double quantum filter (DQF) with four-phase cycling,  $\theta_1 = \theta_2 = \theta_3 = 90^\circ$ ,  $\phi_1 = 0^\circ, 90^\circ, 180^\circ, 270^\circ$ ,  $\phi_2 = \phi_1$ ,  $\phi_3 = 0^\circ$ . For DQF with magic angle (DQF-MA),  $\theta_1 = 90^\circ$ ,  $\theta_2 = \theta_3 = 54.7^\circ$ , and the phase cycling is the same as for DQF. For all filters, the receiver phase alternates between  $0^\circ$  and  $180^\circ$ .

In isotropic liquids only odd rank tensors  $T_{3\pm 1}$  can be formed during  $\tau$  under the influence of quadrupolar relaxation. In anisotropic media, where the RQI does not average to zero, rank tensors  $T_{2\pm 1}$  can be also formed.

A second pulse  $\theta_2$  and phase  $\phi_2$  converts these SQC into multiple quantum coherences (MQC)  $T_{1\pm 1}$ ,  $T_{2\pm 2}$ ,  $T_{3\pm 2}$ ,  $T_{3\pm 3}$ . During the evolution time  $\delta$ , the MQCs evolve with their characteristic relaxation times. Generally, the evolution time  $\delta$  is kept very short to avoid their decay.

Since the MQCs cannot be detected directly, the final RF pulse  $\theta_3$  and phase  $\phi_3$  converts the MQCs into SQCs  $T_{1\pm 1}$ ,  $T_{2\pm 1}$ ,  $T_{3\pm 1}$ , which then evolve under relaxation and RQI to the detectable SQC  $T_{1\pm 1}$  during the acquisition time  $t_{acq}$ . It can be notice that in general, a  $180^\circ$  RF pulse can be applied in the middle of the preparation time  $\tau$  in order to refocus the chemical shifts and magnetic field inhomogeneities. However, as

MQF are very sensitive to RF imperfections, it has been shown that filters without this refocusing pulse generate a better signal and are more robust to RF inhomogeneities for MQF MRI [32]. The formation of DQC and TQC is detected separately by choosing the appropriate RF pulse flip angles and phase cycling. The phase cycling and choice of RF pulses are given in the caption of Fig. 2.6.1. DQF can detect the contribution of two tensors,  $T_{2\pm 1}$ ,  $T_{3\pm 1}$ , due to the slow motion regime or/and RQI in anisotropic media. if  $\theta_1 = \theta_2 = \theta_3 = 90^\circ$ , contributions from both  $T_{2\pm 1}$  and  $T_{3\pm 1}$  can be detected. If  $\theta_1 = 90^\circ$  and  $\theta_2 = \theta_3 = 54.7^\circ$  (magic angle), only the contribution of  $T_{2\pm 1}$  is detected, which arises only from the anisotropic RQI. Only  $T_{3\pm 1}$  due to the slow motion regime can be detected by the TQF sequence.

## 2.7 Fluid and Extracellular Sodium Suppression

In many diseases, a sodium concentration increases is detected, which can be caused by either an increase of intracellular sodium concentration, increase of extracellular volume with a constant



concentration (140 mM) or increase of vascularization. It is widely believed that the most sensitive way to study the health of tissues *in vivo* should be done by isolating the sodium NMR signal from the intracellular compartment. Intracellular sodium concentration and relaxation properties should give access to some more useful information on the cells viability (homeostasis, energetic state and sodium pump function) [33]. Four different techniques have been suggested to suppress extracellular sodium and/or the signal from fluids around the tissue of interest.

### Shift Reagents (SR)

This technique is based on the use of a  $^{23}\text{Na}$  chemical shift reagent based on lanthanide chelates as  $\text{Tm}(\text{DOTP})^{5-}$ ,  $\text{Dy}(\text{PPP})_2^{7-}$  or  $\text{Dy}(\text{TTHA})^{3-}$  [34–36]. These compounds do not penetrate the cell membrane and therefore create a frequency offset for the sodium nuclei in the extracellular space. But as they don't cross the blood-brain barrier and because of their moderate toxicity, these SR can't be used in humans.

### Diffusion

Diffusion-based techniques can separate the sodium signal from the intracellular and extracellular compartments based on the differences between the motional properties of the ions in these two compartments [37]. However, the fast T2 relaxation of sodium and its low gyromagnetic ratio require the use of very large magnetic field gradients, which cannot be effectively implemented in clinical MRI scanners.

### Inversion Recovery (IR)

The IR technique is based on the difference in the T1 relaxation of the sodium nuclei in different compartments. As the T1 relaxation time of the extracellular sodium or in fluid can be significantly longer than the T1 of the intracellular sodium, IR can be used to eliminate the signal contribution from either environment [38–40].

### Multiple Quantum Filters

The MQF technique is based on the different T2 relaxation properties of the sodium nuclei in the intracellular and extracellular or fluid compartments. MQF can be used to differentiate these compartments, as they use coherence transfer schemes to generate an NMR signal that is related to the presence of biexponential relaxation. The MQF are described in the previous section. Depending on the pulse amplitudes and the phase cycling, these filters can allow the signal coming from the sodium DQC or TQC to be read by the sequence. However, the signal intensity

following a MQF sequence is a small fraction of the signal intensity following a single ideal  $90^\circ$  excitation pulse (around 10% has been given as a typical *in vivo* value).

Several reports estimate that the MQF NMR signal in biological tissues comes primarily from the intracellular sodium [41–44], but this statement is still controversial and studies on physiological samples have shown a significant contribution of the extracellular sodium in MQ-filtered spectra [33, 45, 46].

### Applications to Sodium MRI

IR and the MQF are the two only techniques that can be currently applied in sodium MRI *in vivo*. Despite the fact that they cannot really separate completely the different compartments in biological tissues, due to their complex distribution of spectrum types and relaxation times (see Fig. 2.4.1), the resulting signals detected after application of these filters can still contain more signal weighting from certain compartments (intracellular) compared to the others (extracellular, fluid) and thus give some new useful information on the health of the tissue under study.

## 2.8 RF Pulse Sequences

Due to the short (biexponential) T2 relaxation of sodium *in vivo*, ultrashort TE (UTE) sequences are recommended to acquire the images. The first sodium images were acquired with 3D gradient

echo sequences [47] where the TE was minimized by using non-selective hard pulse, in order to avoid using a slice refocusing gradient, and by applying read and phase gradients with the maximum slew rates and magnitudes. TE of the order of 2-3 ms can be obtained with this method. The shortest TEs ( $< 1$  ms) can generally be obtained by acquiring the data from the center of the k-space in a radial or spiral fashion. The most common type of this kind of sequence is the 3D radial sequence which has been used widely for sodium MRI [48]. This method can then be improved from the signal-to-noise ratio (SNR) and time efficiency point of view by modifying the density of acquisition points along the projections and also by twisting the radial projection in the outer k-space in an optimal manner in

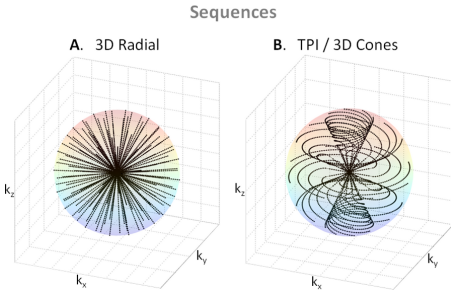


**Figure 2.8.1:** K-space trajectories from UTE sequences. **A.** 3D radial. **B.** Twisted projection imaging (TPI) or 3D cones types of sequences.

order to fill the k-space more homogeneously and improving the point spread function of the acquisition method. This is done in sequences such as density adapted radial sequence [49], twisted projection imaging (TPI) and its variations [15, 50, 51], 3D cones [52] or FLORET [53]. Examples of k-space trajectories from 3D radial and TPI sequences are shown in Fig. 2.8.1. These latter sequences are now the standard for sodium MRI. Other UTE sequences have also

been developed with even shorter TEs, but are still under investigation for about their application to *in vivo* sodium MRI: SPRITE [54, 55], SWIFT [56], ZTE [57], PETRA [58]. The data acquired with all these non-Cartesian sequences are then reconstructed using different methods, such as regridding [59–61] or non-uniform fast Fourier transform (NUFFT) algorithms [62, 63], or iterative methods [64, 65].

## 2.9 Sodium Quantification

Sodium concentration quantification is generally performed by placing phantoms of known sodium concentration and known relaxation times within the field-of-view of the images. It is better to use phantoms with relaxation times that match approximately the relaxation times of the investigated tissue in order to reduce uncertainties in the quantification. A linear regression from the phantom signals, corrected for relaxation, is then used to produce the tissue sodium concentration (TSC) map. For example, reference phantoms for brain or muscle imaging are composed of 2-3% agar gels with sodium concentrations within the range of TSC usually found in these tissues (10 mM up to 150 mM). For cartilage, 4-6% agar gels can be used, with sodium concentration between 100 to 350 mM.

## 2.10 Limitations and Prospects

### Limitations

The low sodium concentration in biological tissues compared to the water concentration, associated with a low NMR sensitivity and very short transverse relaxation times, make the detection of sodium signal quite challenging and result in images with low SNR (around 20-40), low resolution (2-10 mm) and long acquisition times (10-30 min). Moreover, due to the low gyromagnetic ratio of the sodium nuclei (26% of proton gyromagnetic ratio), high magnetic field gradients need to be used for acquiring images with higher resolution, which can therefore be limited by the hardware capacities of the clinical scanners (around 40 mT/m in general). This gradient limitation can also impede studies on sodium ions diffusion with MRI due to the very high gradients needed for detecting even small ion displacements.

Other limitations include the need of high static magnetic fields (>3T) for increasing the sodium signal associated with multinuclear capabilities and the availability of single tuned  $^{23}\text{Na}$  coils or dual-tuned  $^1\text{H} / ^{23}\text{Na}$  RF coils that allow to acquire co-registered proton and sodium images.

### Prospects

Sodium MRI acquisitions could profit from new recent multichannel capabilities developed for rapid proton MRI with parallel data acquisition using array coils and parallel reconstruction algorithms [66], and also new reconstruction schemes such as compressed sensing (CS), that allow rapid undersampled data acquisitions [67]. A optimized combination of parallel-CS-NUFFT reconstruction associated with optimized sequences such as TPI at high field could therefore allow to significantly reduce the acquisition time to a few minutes and still generate images of good resolution (1-2 mm) and reasonable SNR, that would put sodium MRI in the realm of practical clinical imaging techniques.

As assessing the intracellular sodium content can give more useful metabolic information on the integrity of cells, techniques that increase the sensitivity of sodium MRI to this concentration, such as IR or TQF, still need to be improved, in order to increase the SNR, and thus reduce the resolution and acquisition time, of the images, as well as reducing their sensitivities to magnetic field and RF inhomogeneities [68]. A recent new method based on optimal control theory [69, 70] could also prove to be useful for this purpose, but it is still under investigation and has not been applied to *in vivo* sodium MRI yet.

## 3 Biomedical Applications

In this part we will give an overview of the possible biomedical applications of sodium MRI for assessing diseases and therapies non-invasively and quantitatively *in vivo*. Of course, this list of applications is not exhaustive, but we expect it shows a fair spectrum of the research that has been performed over the last 30 years on this subject.

### 3.1 Brain

Since the first experiments on sodium MRI, many studies have been performed on brain, first to show the feasibility of quantitative brain sodium MRI, and then to evaluate its possible use for assessing diseases such as tumors, strokes, multiple sclerosis (MS), Alzheimer's disease (AD) or Huntington's disease (HD), which will be described in this section. The hypothesis is that sodium MRI could provide direct non-invasive information on the changes in cellular integrity/viability through changes in intracellular sodium concentration and/or extracellular volume due to these pathologies, and complement proton MRI or other imaging modalities [12, 14, 71–74]. Examples of SQ and TQF brain sodium images are shown in Fig. 3.1.1 A-B. Some other examples of sodium images with new TQF schemes can be found in Ref. [68, 75, 76] and with IR in Ref. [38, 77].

Thulborn et al. [78] proposed to measure tissue sodium concentration (TSC) and cell volume fraction (CVF) for assessing diseased tissues in the brain (tumor, stroke), along proton MRI. These two parameters are termed "bioscales", as they are quantitative parameters with spatial distribution, while "biomarkers" are often just binary indicators of the presence of disease or not. TSC is the volume fraction weighted mean of the intracellular sodium concentration ( $[Na]_{in} = 10-15$  mM) and the extracellular sodium concentration ( $[Na]_{ex} = 140-150$  mM) and CVF is around 0.8 in normal brain tissues. Therefore  $TSC = CVF \times [Na]_{in} + (1-CVF) \times [Na]_{ex}$ . After correction of the fractional average water content in normal brain as around 0.8, the average TSC in brain is calculated as 45-55 mM, which is the range of values usually measured experimentally. Increasing TSC is supposed to indicate loss of tissue viability while CVF indicates concomitant decrease in cell density. TSC maps can be obtained directly from quantitative sodium MRI where reference phantoms with known sodium concentrations and relaxation times are placed within the FOV.

However CVF cannot be obtained directly, but can be obtained from TSC through knowledge of  $[Na]_{in}$  and  $[Na]_{ex}$ , obtained from TQF sodium MRI for example [79].

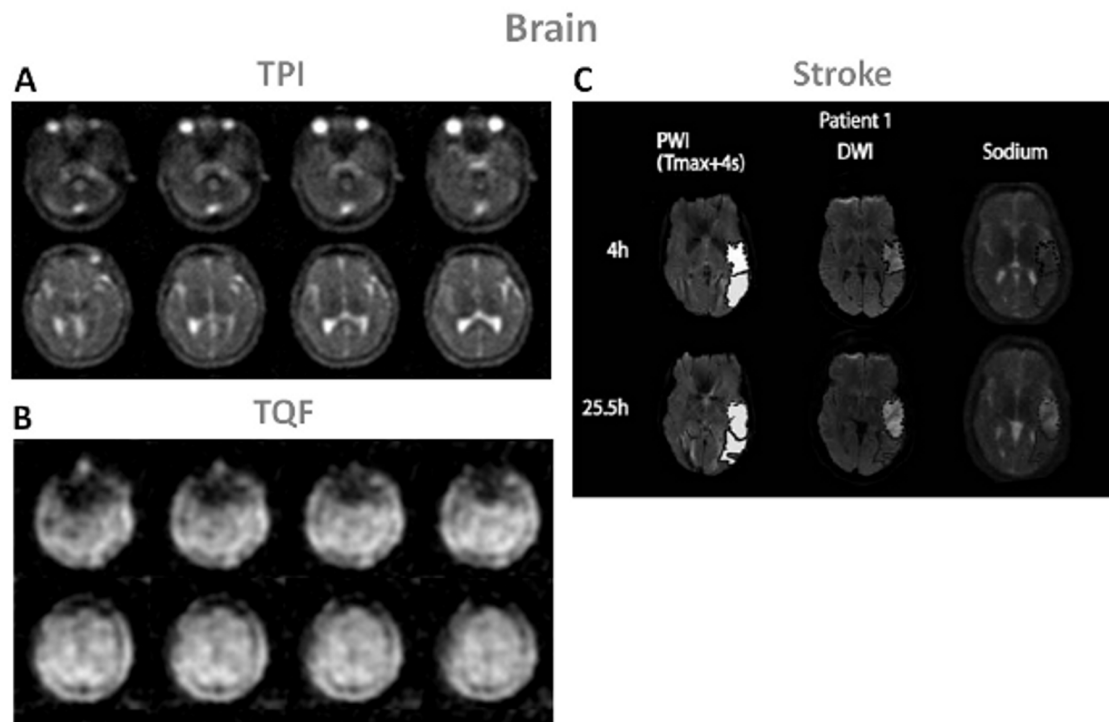


**Figure 3.1.1:** Examples of brain images. **A.** Twisted projection imaging (TPI) at 3T of a healthy brain. **B.** Triple-quantum filtered (TQF)-TPI at 3T of a healthy brain. **C.** Representative perfusion weighted imaging (PWI), diffusion weighted imaging (DWI) at 1.5T and sodium TPI at 4.7T of the brain of a patient with acute ischemic stroke. These images show the hypoperfused (Tmax+4s) perfusion maps, the DWI hyperintense (core) in dotted outline and the PWI-DWI mismatch tissue (penumbra) in solid outline, and corresponding sodium images, acquired 4h and 25.5h after symptom onset. Figures A and B: Courtesy of Professor F. Boada, New York University Medical Center / University of Pittsburgh Medical Center. Figure C from Tsang A. et al. *Journal of Magnetic Resonance Imaging* 33:41 47, 2011. Reproduced by permission of Wiley-Blackwell.

## Strokes

Stroke is the third largest cause of death in the USA and a leading cause of long-term disability. Stroke can be classified in two subtypes: ischemic and hemorrhagic. Most of the strokes are ischemic (around 87 %). It is very important to intervene as early as possible after symptom onset in order to reperfuse viable tissues and minimize tissue loss in order to improve recovery. The usual treatment is thrombolysis by intravenous injection of recombinant tissue plasminogen (tPA) within a 3-hour window after onset [80], which induce recanalization of blocked arteries and potentially reperfusion of ischemic tissues. However, there is a risk also of hemorrhagic transformation or edema formation due to reperfusion in non-viable tissues which can reverse

the expected outcome of thrombolysis. It is therefore important to assess the viability of tissues and their likelihood to recover before treatment is applied.

A combination of proton diffusion weighted imaging (DWI) and perfusion weighted imaging (PWI) [81] has been proposed to help identify patients with more probable improvement in outcome after thrombolysis: ADC maps from DWI can identify regions of cerebral ischemia (water restriction) within minutes after ischemic onset, reflecting cytotoxic edema, and PWI can detect regions with perfusion deficits (regions at risk) within seconds of the ischemic onset. It has been proposed that the mismatch area between a larger abnormal PWI region and a smaller lesion in ADC map can represent the ischemic penumbra, where the tissue is at risk for infarction but still viable, and therefore could be saved [82–84]. However, this PWI-DWI mismatch method has some serious limitations. It has been found that DWI does not necessarily represent ischemic tissue damage, that the limit of salvageable tissue is not limited to the volume of DWI-PWI mismatch, and that PWI and DWI do not provide information on the duration of the acute period of ischemia, and cannot establish the time of symptom onset, therefore unknown-onset patients are excluded from thrombolysis treatment [85, 86].

A more direct method, such as quantitative sodium MRI, that could give accurate spatial information on the tissue viability and also time information about the stroke onset would prove to be very useful for stroke management. TSC is very sensitive to cell homeostasis and any loss of cellular energy production will impair the  $\text{Na}^+/\text{K}^+$ -ATPase and induce loss of ion balance across the cell membrane. An increase in TSC can be associated to increase of intracellular sodium due to the loss of integrity of the cell, and also increase of extracellular volume when cells are dying. Studies in animal model and humans have shown that sodium MRI can measure increases in TSC over the first few hours and days after induction of cerebral ischemia, and that sodium MRI could have a potential utility for stroke management [85–89]. These studies have shown that a elevation of 50% in TSC above the TSC value in the homologous region in contralateral brain hemisphere was consistent with completed infarction, which corresponds to a value of 70 mM in humans. This value could therefore serve as a threshold for tissue viability and help decision making about which treatment should be more adapted for the patient. It is also suggested that the different rates of loss of tissue viability are reflected in the different rates of change in TSC values between cortex and basal ganglia. Therefore, clinical decisions to use thrombolytic agents may use different time windows depending on the location of the stroke. These studies showed that sodium MRI can be used as a useful complement to DWI and PWI for managing patients with acute and subacute stroke and that TSC evolution can help guide thrombolysis protocol outside the 3-hour time window currently used for treatment decision making.

Some examples of sodium images in human stroke are shown in Fig. 3.1.1 C. In this study, Tsang et al. [85] showed that sodium signal intensity cannot be predicted by PWI and that is was

not altered within the PWI-DWI mismatch tissue, irrespective of the interval between symptom onset and image acquisition, indicating preserved viable tissue in this region. A combination of DWI, PWI and sodium MRI could therefore provide useful information on tissue viability in patients with stroke, and thus despite unknown symptom onset time. Further studies are necessary to validate all these findings, with optimized sodium acquisitions with maybe TQF or IR preparation for increasing the weighting of the images towards intracellular sodium content, but sodium MRI seems to be very promising for helping stroke management in a quantitative and non-invasive manner.

## Tumors

Tumor malignancy can be characterized by angiogenesis and cell proliferation [90], among other characteristics. Unregulated cell division, leading to tumor growth, can be initiated by changes in  $\text{Na}^+/\text{H}^+$  exchange kinetics and therefore changes in the intracellular and extracellular pH [91]. This mechanism, associated with reduced  $\text{Na}^+/\text{K}^+$ -ATPase activity [92] leads to increased intracellular sodium concentration that can therefore also be associated with tumor malignancy [93, 94]. Most likely, the increase in total sodium concentration in malignant tumors depends on both changes in extracellular volume fraction and in intracellular sodium content. Similarly, tumor neovascularization and increase in interstitial space both lead to increased extracellular volume fraction and are also associated with the potential for tumor proliferation [95]. Overall, total sodium concentration levels in malignant tumors are likely to be elevated, and therefore could maybe measured by quantitative SQ sodium MRI non-invasively. Implementing TQF or IR in the sodium acquisition could also provide some information more specific to changes in the intracellular sodium content by reducing the weight of fluids (from edema) and/or extracellular sodium in the contrast of the images.

The conventional MRI protocol for brain tumor is based on T2 weighted images and T1 weighted images with and without gadolinium enhancement for detecting the location and dimension of the tumor, DWI for detecting the extent of vasogenic edema while excluding cytotoxic edema and PWI for detecting the regions of the tumor with high vascularity on the relative cerebral blood volume map, which are consistent with high-grade tumor [78]. But all these changes are generally late events in tumor onset. Adding sodium MRI to the protocol would therefore provide direct and more rapid biochemical information on the tumor metabolism, and also help monitor the immediate effects and follow up affects over time of cancer therapies.

Ouwerkerk et al. [94] combined proton and sodium MRI at 1.5T to measure the TSC in brain and determine how TSC is altered in malignant tumors. Sodium images were acquired with a UTE TPI sequence. Mean TSC (in mmol/kg wet weight) was measured as 60 for grey matter (GM), 70



for white matter (WM), 135 for cerebrospinal fluid (CSF), 115 for vitreous humor, 100 for tumor, 70 for unaffected contralateral tissue, and 100 for regions surrounding the tumors (detected with FLAIR hyperintense proton image). Significant differences in TSC were demonstrated for both tumors and surrounding FLAIR hyperintense tissues versus GM, WM, CSF, and contralateral brain tissue. This work shows that UTE sodium MRI can be used to quantify absolute TSC in patients with brain tumors and shows increased sodium concentration of 50-60% in tumors relative to that in normal brain regions. However, these measurements cannot define if TSC increases are due to changes in extracellular volume, intracellular sodium content or neovascularization.

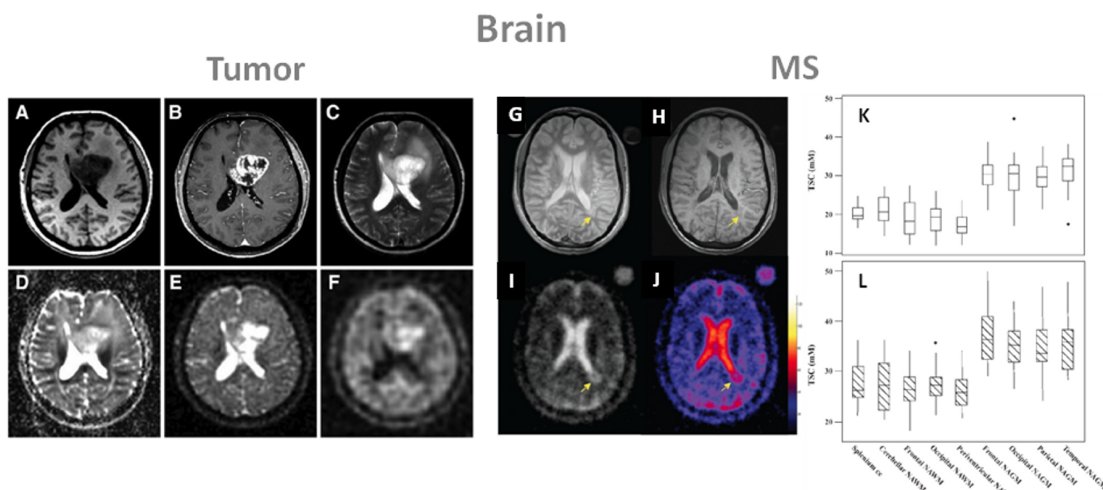


**Figure 3.1.2:** Examples of brain images. **A-F:** Proton and sodium images from a patient with glioblastoma (WHO grade IV) of the left medial frontal lobe. **G-L.** Images and tissue sodium concentrations (TSC) from a patient with multiple sclerosis (MS). **A.** T1 weighted MRI, **B.** T1 weighted MRI with contrast medium (rim enhancement), **C.** T2 weighted MRI showing cystic and solid portions of the lesion and perifocal brain edema, **D.** DWI showing elevated ADC values in the center of the tumor, **E.** sodium MRI showing increased sodium signal in the tumor, **F.** sodium MRI with fluid suppression by inversion recovery (IR), also showing increased sodium signal mainly at the center of the tumor. Proton images (**A-D**) were acquired at 3T while sodium images (**E, F**) were acquired at 7T. **G.** proton density MRI, **H.** T1 weighted MRI, **I.** sodium MRI, **J.** corresponding TSC map. **K.** box-plot of the mean TSC value distribution in regions of white matter and grey matter in healthy controls. **L.** box-plot of the mean TSC value distribution in regions of the corresponding normal appearing white matter (NAWM) and normal appearing grey matter (NAGM) in patients with relapsing-remitting MS. Abbreviation: cc is corpus callosum. Figures A-F from Nagel A. et al. *Investigative Radiology* 46(9), 539-547, 2011. Reproduced by permission of Wolters Kluwer Health. Figures G-L from Inglese M. et al. *Brain* 133, 847-857, 2010. Reproduced by permission of Oxford University Press.

Nagel et al. [77] recently applied sodium MRI with and without IR to 16 patients with brain tumors of different grades (WHO grades I-IV) at 7T. Some examples of proton and sodium images are presented in Fig 3.1.2 A-F. Their findings were that TSC imaging revealed increased signal intensities in 15 of 16 brain tumors before therapy and that IR imaging enabled further differentiation of these lesions by suppressing CSF and edema signal; all glioblastomas (grade IV) demonstrated higher IR sodium signal intensities as compared with WHO grade I-III tumors.

It was also noted that contrarily to total TSC signal, the IR sodium signal correlated with the histologic MIB-1 proliferation rate of the tumor cells. This study shows that a combination of sodium MRI with and without T1 relaxation weighting through IR can reveal important physiological tissue characteristics and help characterize and grade tumors.

Very recently Fiege et al. [75] combined SQ and TQF sodium imaging in a single acquisition scheme and applied this new sequence to 6 healthy brains and 3 brains with tumors at 4T. In this very preliminary work, they detected a decrease of signal in tumor regions on the TQF images compared to normal tissue, probably due to suppression of edema around the tumors. But due to the very low resolution of the images (10 mm isotropic) and low SNR of the TQF images, it is hard to reach any definitive conclusion yet.

### Multiple Sclerosis

Another interesting application of sodium MRI in the brain would be for assessing multiple sclerosis (MS). MS is an inflammatory neurological disease characterized by focal and diffuse inflammation in white matter (WM) and grey matter (GM), by demyelination of the axons and by neuro-axonal injury and loss, but the cellular and molecular mechanisms contributing to neurodegeneration are still poorly understood [96]. Studies have shown that the accumulation of sodium in axons through non-inactivating sodium channels can promote reverse action of the  $\text{Na}^+/\text{Ca}^{2+}$  exchanger, which leads to a metabolic cascade, and results in an overload of intra-axonal calcium and axon degeneration [97, 98].

Inglese et al. [99] recently demonstrated the first application of sodium MRI to MS at 3T in 17 patients with relapsing-remitting MS (rrMS) and 13 normal subjects. The main results are shown in Fig. 3.1.2 G-H. Images were acquired at 3T with a 3D radial sequence and a birdcage coil. The absolute TSC was measured in lesions and in several areas of normal-appearing white and grey matter in patients (NAWM and NAGM in proton MRI), and corresponding areas of white and grey matter in controls. Mean sodium concentrations were 20 and 30 mM in WM and GM in controls, and 27 and 36 mM in corresponding NAWM and NAGM in MS patients. In this preliminary study, TSC in MS patients issue were therefore elevated in acute and chronic lesions compared to areas of NAWM. The TSC in areas of NAWM were significantly higher than those in corresponding WM regions in healthy controls. TSC averaged over lesions and over regions of NAWM and NAGM matter was positively associated with T2-weighted and T1-weighted lesion volumes from proton MRI. The expanded disability status scale score showed a mild, positive association with the mean TSC in chronic lesions, in regions of NAWM and NAGM. More studies need to be performed to understand the pathophysiological mechanisms involved in tissue injury in MS and their link to sodium images. Separation of intracellular and extracellular sodium by TQF [79] or IR could

prove to be useful for this purpose. But this work shows that abnormal values of TSC measured non-invasively with sodium MRI in patients with rrMS might reflect changes in the composition of the lesions and/or changes in metabolic integrity.

Another recent study by Zaaraoui et al. [100] expanded the method to patients with early and advanced rrMS. It was found that TSC increased inside demyelinated lesions in both groups of patients. TSC was also increased in NAMW and NAGM of advanced rrMS patients, but not in early rrMS.

### **Alzheimer's Disease**

Finding biomarkers for detecting early signs of AD and tracking response to treatments is a subject of intense research. Methods such as sampling the cerebro-spinal fluid (CSF) for biochemical analysis of biomarkers, positron emission tomography (PET), and MR imaging (through regional volumetric analysis) or spectroscopy (N-acetylaspartate with  $^1\text{H}$  NMR or glutamate with  $^{13}\text{C}$  NMR) have been proposed.

A first study on the applicability of sodium MRI to Alzheimer's disease (AD) was performed by Mellon et al. [101]. The hypothesis here is that alterations of the sodium levels in brain due to cell death or loss of viability characteristics of AD could be measured with sodium MRI non-invasively and give useful complementary information for assessment of early AD. They did not quantify the sodium concentrations but still were able to detect a small increase (7.5%) of the sodium relative signal intensity in the brains of patients with AD compared to controls and found that this signal intensity enhancement was moderately inversely correlated with hippocampal volume measured from T1 weighted inversion recovery proton images. No conclusive explanation on a physiological basis can be advanced for explaining this sodium content increase. Is it due to increase of extracellular volume due to cell death and fluid invasion, increase of intracellular sodium due to an impairment of  $\text{Na}^+/\text{K}^+$ -ATPase, leakage of sodium due to amyloid beta channels in the membrane, or probably a combination of many of these causes? More studies that allow fluid suppression and/or intracellular sodium isolation (IR, TQF) should be performed in order to selectively study these possible aspects of AD progression.

### **Huntington's Disease**

A very recent preliminary study [102] showed that patients with Huntington's disease ( $n=13$ ) also present an increased of TSC in the whole brain compared to healthy controls ( $n=13$ ), in structurally affected regions of the brain, but also in some non-affected regions. As for the AD study, no satisfying explanation to these TSC increases could be proposed due to the limited data, low resolution and lack of differentiation between intracellular and extracellular sodium content.

But further more complete studies may help explain these observed TSC variations which are generally linked to changes in cellular and metabolic integrity leading to structural degeneration.

## 3.2 Breast

Treatments for breast cancer such as prophylactic mastectomy or chemoprevention are more effective when the disease is detected at an early stage. The most common techniques for detecting breast cancer are clinical breast exam (CBE), ultrasound and x-ray mammography. Mammography has a high sensitivity (70-90%) but a limited specificity (32-64%) leading to many false positives, and very often cannot distinguish benign from malignant tumors [103]. Moreover, approximately 10% of tumors are not detected by mammography due to the presence of dense fibroglandular tissue. Adding ultrasonography to mammography can help increasing the sensitivity but also increases the number of false positives [104].

Proton MRI, particularly contrast-enhanced and diffusion MRI, is a promising technique for detecting and characterizing tumors not visible in mammograms, mainly in dense tissues, as MRI has a very high negative predictive value (rule out the presence of cancer) [105]. But the specificity of proton MRI could be improved by adding more information about the physiology and metabolism of suspicious lesions, such as cellular integrity and energy metabolism. As proliferating tumors may cause increases in the sodium content of tissues due to disruption of the sodium-potassium pump in cell membranes, quantitative sodium MRI would be a good candidate to detect tumors in the breast and also assess the degree of malignancy and follow-up chemotherapy. To test this hypothesis, Ouwerkerk et al. [106] applied quantitative sodium MRI at 1.5T and TPI acquisition to patients with benign and malignant breast tumors before biopsy. T2 and T1 weighted contrast-enhanced proton MRI were also acquired. Sodium and proton images were co-registered to allow quantification of TSC in normal and suspicious tissues based on  $^1\text{H}$  MRI contrast enhancement, with histology confirmed by biopsy. The measured TSC were higher by an average of 60% in histologically proven malignant lesions compared to glandular tissue. TSC in benign tumors was significantly higher than adipose tissue but on the same level than glandular tissue (34 mM). An example of these results is shown in Fig. 3.2.1.

Increased TSC can arise from increase of extracellular volume fraction (EVF) due to changes in cellular organization, from increase of vascular volume, or from increases in the intracellular sodium concentration due to impaired energy metabolism in  $\text{Na}^+/\text{K}^+$ -ATPase activity, or a combination of all these causes. It is therefore impossible from this data to reach any conclusion about the measured elevated TSC, but more studies at higher field, higher resolution, with a combination of sodium sequences allowing to increase the weight of intracellular or extracellular sodium on the images (such as TSC or IR), combined with sensitive proton MRI techniques

such as DWI or T1 contrast enhanced, may allow to increase the sensitivity and specificity of MRI in detecting and assessing biochemical information in breast cancer.

A multiparametric multinuclear combination of MRI techniques could prove to be useful for grading benign and malignant tumors, and also for monitoring chemotherapy response [107]. It was even shown by Jacobs et al. [108] that a multimodal combination of  $^1\text{H}+^{23}\text{Na}$  MRI with computed tomography (CT) and proton emission tomography (PET) was feasible and may help to evaluate the complex tumor micro-environment by examining changes in morphology, sodium concentrations and glucose metabolism in response therapy.

### Breast Cancer

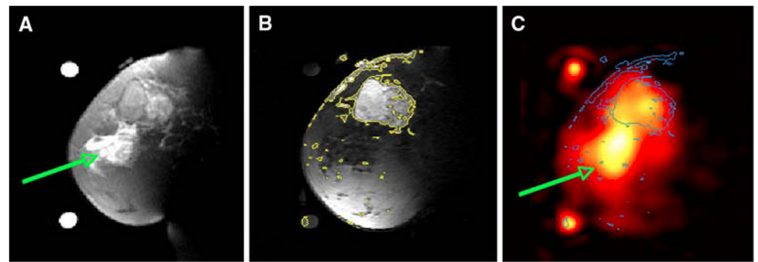


**Figure 3.2.1:** Examples of breast cancer images from a patient with 5.5 cm infiltrating poorly differentiated ductal carcinoma (T3) at the 12 o'clock position in the left breast. **A.** Fat suppressed T2 weighted MRI showing a mass with T2 intermediate signal and edematous T2 bright retroareolar glandular tissue (arrow). **B.** Fat suppressed T1 weighted MRI post-Gd injection with contour levels in yellow, showing enhancement of the mass at 12 o'clock but not in the retroareolar glandular tissue. **C.** Sodium MRI with contours from B superimposed in blue. Region with edema is indicated by the green arrow. From Ouwerkerk R. et al. Breast Cancer Res Treat DOI 10.1007/s10549-006-9485-4, 2007. Reproduced by permission of Springer Science and Business Media.

## 3.3 Heart

Acute myocardial infarction (MI) can lead to an increase in the intracellular sodium concentration due to loss of ionic homeostasis, and to enlarged extracellular volume due to myocardial edema formation or due to scar formation [109, 110]. Quantitative sodium MRI seems therefore a good candidate to try to detect cardiac infarction by measuring localized increased sodium content in cardiac tissues and help differentiate viable from non-viable tissues. Some preliminaries studies using surface coils were performed over the years to test the feasibility of cardiac sodium MRI and to try to assess infarction [47, 111–114].

Ouwerkerk et al. [112] measured the myocardial TSC of healthy volunteers. Mean TSC was approximately 43 mM in the left ventricular (LV) free wall, 53 mM in the septum and 17 mM in adipose tissue. The same team then applied the method to twenty patients with nonacute MI. Mean TSC for MI was measured as 30% higher than noninfarcted tissues in LV regions (significant difference). The mean TSC in regions adjacent to MI regions was intermediate between MI and normal tissue sodium content. They also conclude that TSC increase is not related to infarct age, size or global ventricular function. The measured sodium TSC or pixel intensity changes may be attributable to loss of cellular integrity, inhibition of the  $\text{Na}^+/\text{K}^+$ -ATPase function due to energy depletion and changes in the sodium concentration gradient between intracellular and extracellular volumes, and also possibly changes in the sodium ion molecular environment, and

probably a combination of all.

Because of the methods used until now, it is difficult to find in which proportion and when these probable physiological changes can be associated with observable changes in sodium content or relaxation. Future studies might include imaging at higher fields for increasing the SNR and spatial resolution for better identification of infarcted tissues and adjacent areas, and sequences that could separate intracellular from extracellular sodium and/or relaxation times weighted (TPI associated with TQF or IR), for a better estimation of intracellular TSC, which is generally supposed to be more sensitive to cell energy impairment and viability.

## 3.4 Muscle

Sodium MRI has the potential to provide insights into muscle physiology and for assessing muscle diseases. In muscle tissues, the electrochemical gradient across the cell membrane is maintained by the  $\text{Na}^+/\text{K}^+$ -ATPase, but when an action potential leading to muscle contraction is generated, there is a rapid influx of sodium ions and efflux of potassium ions via the sodium and potassium channels. During intense contractile activity, the persistent influx and efflux of ions, which degrades the transmembrane  $\text{Na}^+$  and  $\text{K}^+$  gradients, can lead to a loss of membrane excitability and muscle contractility [115], which is believed to represent one of the main mechanisms of muscle fatigue [116].

It has already been shown that many disease states, such as diabetes, starvation and hypothyroidism, can be linked to a decrease in  $\text{Na}^+/\text{K}^+$ -ATPase activity in skeletal muscle [115]. Therefore sodium MRI has the potential to play a role in imaging of these disorders. For example, Bansal et al. [117] studied the change of sodium concentration and relaxation in muscle after voluntary muscle contractions. They showed that the sodium intensity in the images increased by around 34% in the exercised muscle and then diminished with a half-time of 30 min, but that the calculated sodium concentration did not change significantly, while the long T2 component of the sodium relaxation increased. They therefore suggest that the change in intensity in the sodium images was mainly due to a change in the sodium-macromolecules interaction rather than a change in TSC. We present in the following paragraphs a few examples of studies of sodium MRI for different muscular diseases.

### Diabetes

Sodium MRI has been applied recently on diabetic patients. Some results from the study by Chang et al. [118] are presented in Fig. 3.4.1. Pre- and post-exercise sodium intensity (SI) was measured in sodium images in healthy volunteers and patients with diabetes, in the tibialis



anterior (TA) as control muscle, in soleus (S) and in gastrocnemius (G) muscles. It was found that the muscle sodium signal intensities (in S and G) increase significantly immediately after exercise and that afterwards this sodium signal recovers down to baseline more slowly in diabetics than in healthy subjects.

The authors suggest that the biophysical basis for the increase in sodium signal intensity in muscle after exercise is probably multifactorial and could be due mainly to 2 main factors: (1) an increase in total muscle sodium content due to increase in volumes of the intracellular and extracellular compartments after exercise and to the increase of intracellular concentration muscle cell depolarization, therefore, the increase in sodium signal intensity following exercise could reflect changes in the quantity of sodium in both compartments; (2) alterations in sodium macro-molecular environment and therefore changes in T2 relaxation times or in the proportions of the long and short T2 components. One possible explanation might be the decreased  $\text{Na}^+/\text{K}^+$ -ATPase activity as well as the altered tissue microvasculature in diabetics.  $\text{Na}^+/\text{K}^+$ -ATPase preserves the muscle membrane excitability by maintaining the  $\text{Na}^+$  and  $\text{K}^+$  concentration gradients across the cell membrane and therefore helps protect muscles against fatigue [115]. However, diabetics have a decreased  $\text{Na}^+/\text{K}^+$ -ATPase activity and decreased numbers of  $\text{Na}^+$  and  $\text{K}^+$  pumps on the muscle cell membrane, which has been attributed to insulin resistance [119]. This would result in a decreased ability to extrude intracellular sodium ions into the extracellular space and result in elevated muscle sodium intracellular content with a slower recovery to baseline.

This preliminary study shows that sodium MRI could therefore be applied to patients with diabetes in order to evaluate those who are at risk of diabetic muscle infarction, which is a grave complication of longstanding diabetes. Moreover, fluid and/or extracellular sodium suppression by TQF or IR, along with T2 relaxation measurements, could prove to be useful to assess the origin of the SI decrease observed in this study.

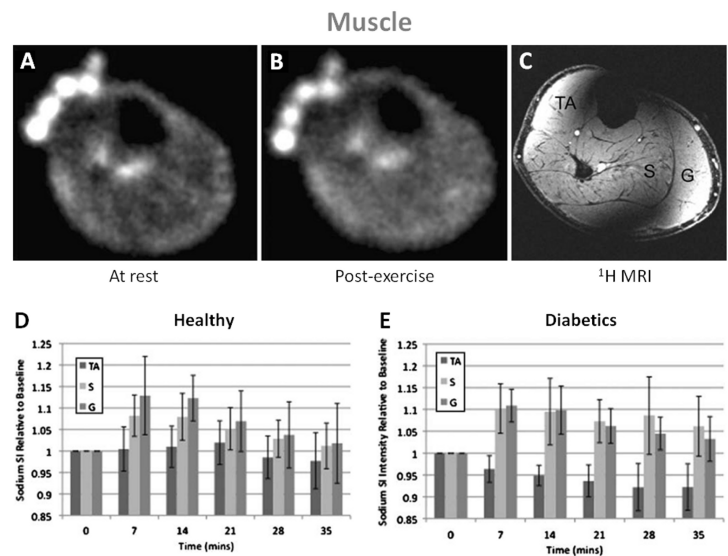


**Figure 3.4.1:** Example of sodium images in the muscle at rest (A) and post-exercise (B). 3D FLASH proton MRI (C) was performed after the sodium MRI to delineate muscle anatomy: TA is tibialis anterior, S is soleus and G is gastrocnemius. In healthy subjects (D), sodium signal intensity increases significantly in S and G just after exercise, but not in the control muscle TA. The sodium intensity then decreases to near baseline in both S and G with a half-time of around 22 min. In diabetics subjects (E), sodium signal intensity increases significantly in S and G just after exercise, but not in the control muscle TA. The sodium intensity then decreases to near baseline half-times of around 37 min in S and 27 min in G. From Chang G. et al. European Radiology, DOI 10.1007/s00330-010-1761-3, 2010. Reproduced by permission of Springer Science and Business Media.

#### Muscular Channelopathy

Patients with hypokalemic periodic paralysis (hypoPP) or paramyotonia congenita (PC), two different kinds of muscular channelopathies, were scanned with sodium MRI in a study by Nagel et al. [120]. These rare diseases are considered to be caused by genetic mutations of the voltage-gated sodium channels in muscular cells, and that can be characterized by elevated myoplasmic sodium at rest and after cooling (for provoking PC pathology effects).

Three sodium techniques were used to assess the disease: total tissue sodium concentration ( $^{23}\text{Na}$ -TSC), T1 weighted sodium imaging ( $^{23}\text{Na}$ -T1) and inversion recovery ( $^{23}\text{Na}$ -IR) which was used to suppress most of the extracellular and vascular sodium and vasogenic edema. All  $^{23}\text{Na}$  sequences showed significantly higher signal intensities in hypoPP compared with PC patients and healthy subjects, and provocation in PC induced a significant increase (>20%) in the  $^{23}\text{Na}$ -IR signal and a corresponding decrease of muscle strength. Signal intensities from  $^{23}\text{Na}$ -T1 and  $^{23}\text{Na}$ -TSC also have a non-significant tendency to be higher after provocation in PC. This study indicates that  $^{23}\text{Na}$ -IR could provide a stronger weighting toward intracellular sodium than  $^{23}\text{Na}$ -T1 or  $^{23}\text{Na}$ -TSC, and therefore may allow a better visualization of changes in intracellular sodium content. A combined application of  $^{23}\text{Na}$ -TSC and  $^{23}\text{Na}$ -IR could therefore improve the analysis of pathophysiological changes in muscles of patients with muscular channelopathies by measuring the changes in intracellular concentration and T1 relaxation time.

The same kind of study was also performed on patient with hyperkalemic periodic paralysis (hyperPP) by Armateifo et al. [121]. They showed that sodium MRI can detect increased myoplasmic sodium content in HyperPP patients with permanent weakness, as they are affected by an incomplete inactivation of muscular sodium channels [122]. In this case too,  $^{23}\text{Na}$ -IR is more sensitive to intracellular changes than  $^{23}\text{Na}$ -TSC and  $^{23}\text{Na}$ -T1. In conclusion, sodium overload may cause muscle degeneration developing with age and sodium MRI could therefore help monitoring medical treatments that reduce this overload.

#### Myotonic Dystrophy

Myotonic dystrophy has been linked to alterations in sodium channel conductance regulation, which can cause elevated muscle fiber concentrations that correlate with disease severity [123].

Constantinides et al. [124] have found in their study that the mean TSC measured with sodium MRI after exercise were elevated by 16% and 22% in two healthy volunteers, and 47% and 70% in two dystrophic muscles in compared with those at normal resting levels. These results in patients with myotonic dystrophy are consistent with the known imbalance in sodium homeostasis in dystrophic muscle fibers [125]. Quantitative sodium imaging could be a valuable tool for characterizing the early onset, pathogenesis, and monitoring of pharmacologic treatment



of dystrophic muscle, but more data need to be acquired to confirm these findings.

## Hypertension

Another interesting possible application of quantitative sodium MRI in muscle is to measure the increase of body sodium content due to hypertension, which is linked to a disturbed total body sodium regulation.

Kopp et al. [126] measured sodium content in triceps surea of healthy volunteers and of patients with primary aldosteronism, before and after treatment. They found a 29% increase in muscle  $\text{Na}^+$  content in patients with aldosteronism compared with normal women and men. This tissue  $\text{Na}^+$  content was then reduced to normal levels (20-25 mM) after successful treatment without accompanying weight loss. They suggest that sites such as muscle (and also skin) could serve to store  $\text{Na}^+$  nonosmotically by binding of the  $\text{Na}^+$  ion to proteoglycans within the extra-cellular compartment without apparent accompanying fluid retention or changes in serum  $\text{Na}^+$  concentration in patients with primary aldosteronism.

Sodium MRI in muscle may therefore be useful for detecting and follow up treatment of hypertension and also help testing the role of  $\text{Na}^+$  for assessing long-term cardiovascular risk in populations.

## 3.5 Cartilage

Cartilage is a dense connective tissue that can be found in many parts of the body such as articular joints between bones (hyaline cartilage), in the ear and nose (elastic cartilage) or in intervertebral disk (fibrocartilage).

In this review article we will mainly focus on articular hyaline cartilage, which consists of a small population of chondrocytes (5% of volume) within a large extracellular matrix (ECM) made of type II collagen fibers (15 20% of the volume), proteoglycans (PG; 3 10%) and water (65 80%) and does not contain blood vessels. PGs further consist of a protein core and negatively charged glycosaminoglycan (GAG) side chains, which endow the cartilage with a negative fixed charge density (FCD). This FCD attracts free-floating positive counter-ions, such as sodium  $^{23}\text{Na}^+$ , which in turn attract water molecules within the cartilage through osmotic pressure. Therefore, we can notice that unlike most of biological tissues, sodium ions in cartilage are mostly present in the extracellular volume. The negative charge from the GAG side chains also provides a strong electrostatic repulsive force between the PG molecules and is responsible for the compressive stiffness of cartilage. The collagen fibers serve to immobilize the PG and provide a tensile force opposing the tendency of the PG to expand the cartilage. Thanks to these

properties, articular cartilage can provide synovial joints with lubrication and also serve to absorb mechanical shocks and to distribute load over the underlying bone, and thus makes normal motion of possible [27, 127].

## Osteoarthritis

Osteoarthritis (OA) is the most common form of arthritis in synovial joints and a leading cause of chronic disability, mainly in the elderly population. From the biochemical point of view, OA is a degenerative disease of the articular cartilage mainly characterized by a reduction of FCD (or GAG) concentration, possible changes of size and organization of the collagen fibers, aggregation of the PG and increased water content. These changes lead to an alteration of the mechanical properties of the cartilage, which can therefore lose its load- and shear-bearing functions. At present, there is neither a known cure nor a preventive treatment for OA, and present treatments focus mainly on pain management with analgesics and improvement in quality of life (e.g., exercise and weight loss). If these methods are ineffective, joint replacement surgery may be considered. Early detection of OA, prior to irreversible morphological changes, and an accurate method for quantifying the effects of potential treatments are therefore of fundamental importance.

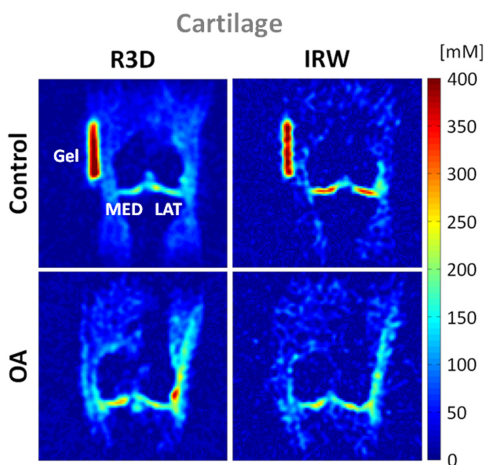


**Figure 3.5.1:** Cartilage sodium concentration maps from a healthy volunteer (control) and a patient with osteoarthritis (OA). Images were acquired with 3D radial (R3D) and IR WURST (IRW). IR WURST was used to suppress fluids through inversion recovery (IR) with an adiabatic WURST pulse in order to increase the sensitivity of the method to change of sodium concentration within the cartilage only. MED = femoro-tibial medial and LAT = femoro-tibial lateral cartilage.

Radiography is the standard method used to detect gross loss of cartilage by measuring narrowing of the distance between the two adjacent bones of a joint, but does not image cartilage directly. Proton MRI, such as T1-weighted, T2-weighted and proton density, can provide morphological information on damage of cartilage, such as fissuring and partial- or full-thickness cartilage defects, but does not give any information on the GAG content within the ECM or the structure of the collagen fibers network. New methods for functional proton MRI of the cartilage are under now development, such as T1 $\rho$  mapping [128], T2 mapping [129], GAG chemical exchange saturation transfer (gagCEST) [130], delayed gadolinium enhanced MRI of cartilage (dGEMRIC) [131] and diffusion weighted imaging (DWI) [132]. T2 mapping and DWI can give information about the collagen fibers and water mobility, while the other methods can give some information about the FCD or GAG content, indirectly through the use of a contrast agent (dGEMRIC), or directly (T1 $\rho$  mapping, gagCEST). All these methods are still under investigation for assessing their specificities and sensitivities for detecting early OA.

It has been shown that sodium concentration has a strong correlation with FCD and GAG content in cartilage [133], therefore quantitative

sodium MRI could also be useful for detecting directly loss of GAG in early OA [134–136]. Several studies have already been performed on healthy and OA cartilage, and show that in general TSC in healthy cartilage is in the range 250–350 mM, while <250 mM in OA cartilage [136]. Because of the low resolution of the sodium images (>3 mm), due to the presence of synovial fluid or joint effusion and also possible cartilage thickening, the sensitivity of the method to measure small changes of TSC within the cartilage only should include fluid suppression by either TQF [137] [17, 137] or IR [39, 138].

An example of quantitative sodium MRI of cartilage at 7T is presented in Fig. 3.5.1, where fluid suppression was obtained by IR with an adiabatic inversion pulse [39]. Images were acquired with a 3D radial sequence. It is shown that fluid suppression allows a better differentiation between control and OA patient. This work is still preliminary but it is reproducible and repeatable [139]. Another possible application under investigation would be the measurements of the relaxation times of sodium in cartilage, which are expected to be very sensitive to any change of their environment, such as GAG depletion of collagen fibers rupture. Some reviews on the potential of sodium MRI and OA are presented in Ref. [27, 140].

### Cartilage Repair

Sodium MRI could also prove to be useful for assessing cartilage repair. Trattinig et al. [141] showed the feasibility of dGEMRIC and sodium MRI at 7T for differentiating repaired tissue after matrix-associated autologous chondrocyte transplantation (MACT) from native cartilage at 3T. A strong correlation was found between sodium imaging and dGEMRIC in patients after MACT. Another recent study by Chang et al. [142] showed that the method for assessing sodium concentration in cartilage repair can be improved by fluid suppression by IR.

### Intervertebral Disk

Insko et al. [143] demonstrated the feasibility of sodium MRI of the intervertebral disk (IVD) *in vivo* at 4T using a surface coil and 3D gradient echo sequence. This technique could be used to measure the proteoglycan content in fibrocartilage and help detect early degenerative changes in IVD. In a subsequent recent study, Wang et al. [144], showed that sodium MRI can correlate with loss of proteoglycans in the spine.

## 3.6 Abdomen

Quantitative sodium MRI could also prove to be useful for assessing cell viability in abdominal organs and in order to detect and diagnose diseases in liver, gallbladder, pancreas, kidney, spleen,

prostate, uterus or other organs [145]. Very few studies have been performed for the moment on the abdomen, mainly due to the lack of availability of body sodium coils and the necessity for the acquisition sequences to take into account the cardiac and respiratory movements of the body, which can seriously perturb the quality of the images. However, some preliminary work is presented here on kidney, prostate and uterus.

## Kidney

The kidney is essential in regulating homeostatic functions in the body such as extracellular fluid volume, acid-base balance (pH), electrolyte concentrations, and blood pressure (via maintaining salt and water balance). This role depends tightly on the regulation of extracellular sodium in the kidney, which builds up a concentration gradient from the cortex to the medulla. Thus renal function is tightly dependent on this corticomedullary gradient and mapping this gradient with sodium MRI could help assess kidney impairments.

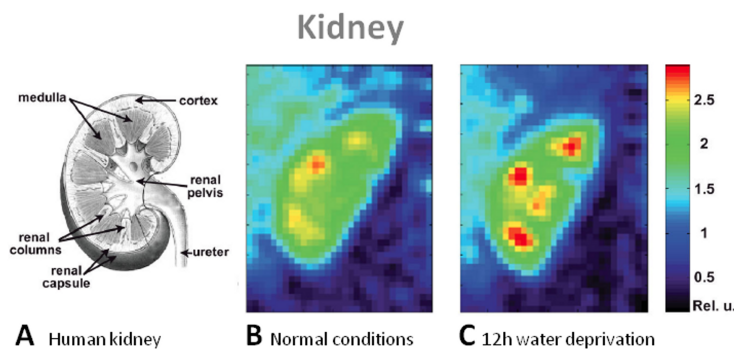


**Figure 3.6.1:** Examples of kidney images. **A.** Scheme of a human kidney. Central coronal slices of the 3D sodium images of a human kidney under normal conditions (**B**) and 12-h water deprivation (**C**). The sodium gradient increases significantly by 25% after water deprivation. From Maril N. et al. *Magnetic Resonance in Medicine* 56, 1229–1234, 2006. Reproduced by permission of Wiley-Blackwell.

A first study in human by Maril et al. [146] presents sodium MRI of kidneys before and after water deprivation, as shown in Fig. 3.6.1. This work was performed at 3T with a surface coil and data was acquired with a 3D gradient echo sequence. The results show that the sodium signal intensity increased linearly from the cortex to each of the medullae with a mean slope of 1.6 (in arbitrary units per mm) and then decreased toward the renal pelvis. After 12 hour water deprivation, this gradient increased significantly by 25%. The sodium gradient change in the kidney may reflect changes in the concentration in each kidney compartment (cortex, medulla), but also micro-compartments within these compartments

(intracellular, extracellular, vascular), differences in the relaxation times of sodium within the tissues, or a combination of all of them.

A following study by Rosen et al. [147] performed sodium MRI at 3T on a patient with a transplanted kidney, who was previously diagnosed with end-stage hypertensive nephropathy, to measure the corticomedullary sodium gradient and to assess the good functioning of the new kidney. The kidney was imaged 4 months after transplantation. The measured mean medulla/cortex SNR ratio was of 1.8, and the gradient slope was 1.1 (arbitrary units / mm), which is lower than

the gradient observed in healthy kidney in the previous study. A interpretation can be made at this stage as the kidney was recently transplanted, resolution and SNR were low and the physiology/biochemistry involved are not fully known. More studies need to be done of course, but these findings are encouraging for a possible application of quantitative sodium MRI for assessing renal functions in different diseases such as nephropathy, renal failure and kidney transplantation.

### Prostate

Sodium MRI of the human prostate was recently tested *in vivo* at 3T [148, 149] and compared with diffusion MRI. The prostate and its different departments were identifiable, with measured TSC of around 60 mM in the central zone and 70 mM in the peripheral zone. This method could be a potential radiological biomarker of prostate cancer and of treatment response.

### Uterus

Uterine leiomyomata (fibroids) were investigated by diffusion weighted imaging (DWI) and quantitative sodium MRI by Jacobs et al. [150] at 1.5T. Uterine leiomyomata are solid masses arising from the muscle of the uterus (myometrium) and can be associated with menstrual pain and loss of reproductive function. The goal was to monitor the treatment of fibroids on patients that were treated using MRI guided high-intensity focused ultrasound surgery (MRg-HIFUS). Regions where the tissue was treated were clearly identified on both DWI and sodium images. The TSC in normal myometrium tissue was approximately 36 mM with apparent diffusion coefficient (ADC) of 2.2 mm<sup>2</sup>/s. The TSC was 28 mM in untreated fibroids and increased to 42 mM in treated tissues while ADC was 1.75 mm<sup>2</sup>/s in untreated fibroids and decreased to 1.3 mm<sup>2</sup>/s in treated tissues.

The mechanisms involved in the changes in ADC and TSC in treated uterine tissue is still unknown but these changes may provide an empirical measure of the efficacy of the treatment. DWI is sensitive to translational motion and changes in the intra- and extracellular compartments available for diffusion of water molecules and can reveal disruptions or restrictions to the movement of these molecules within a tissue. Sodium MRI is more sensitive to the gradient of ion concentration between the intra- and extracellular compartments, which depends on the Na<sup>+</sup>/K<sup>+</sup>-ATPase activity within the cell membrane and its energy consumption. Thermal ablation disrupts the cell membrane and alters the cellular integrity and perfusion of the tissue. The ADC and sodium changes within the diseased uterine tissue before and after treatment may therefore reflect a combination of complex changes in tissues such as modification of the water environment, disruption of Na<sup>+</sup>/K<sup>+</sup>-ATPase function, decreased vascularization or cytotoxic edema. More data must be acquired to fully understand these findings, but this preliminary study suggests that DWI (ADC map) coupled with quantitative sodium concentrations may provide useful non-invasive biomarkers for

uterine leiomyomata response to therapy or to investigate malignant tumors, by probing biochemical changes that can give information beyond the usual anatomical imaging parameters.

## 3.7 Whole Body

Most of human parts have been scanned with sodium MRI separately for the moment, and recently a study by Wetterling et al. [151] showed a whole body sodium MRI *in vivo* at 3T. A new asymmetrical birdcage coil was used to acquire the data in 5 segments of 10 min each with a 3D radial sequence, and a nominal isotropic resolution of 6 mm. The resulting composite image of the 5 acquisitions is shown in Fig. 3.6.2. Despite the low resolution, we can easily detect many different organs such as the brain, the left and right ventricles of the heart, the liver, the bladder, the spine or articular cartilage. A possible application of whole body sodium imaging would be for example the detection and malignancy assessment of cancer with metastases, and follow-up of the chemotherapeutic response.

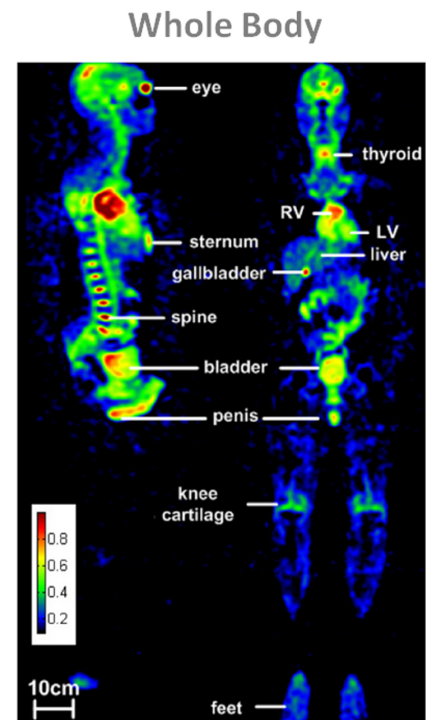


**Figure 3.6.2:** Whole body sodium MRI of a volunteer. From Wetterling N. et al. Phys. Med. Biol. 57, 4555-4567, 2012. Reproduced by permission of IOP Publishing Ltd.

## 3.8 Cancer and Chemotherapeutic Response

Although the following studies were not performed on humans but on rats or mice *in vivo*, it is useful to mention them as they represent an important preliminary work previous to potential human applications on cancer and chemotherapeutic response assessment [40, 152, 153]. The goal of cancer therapy is to eliminate neoplastic cells, but assessment of the therapeutic efficiency *in vivo* may be difficult. Different functional imaging modalities such as PET (rate of glycolysis), DWI MRI (extracellular volume) or sodium MRI (intracellular sodium) could prove to be useful for this purpose.

### Chemotherapy Assessment

It has already been demonstrated that DWI can be useful for quantitative assessment of tumor response to therapeutic insult by observing the microscopic changes in water diffusion due to cellular destruction and that is highly sensitive to microscopic changes in cellular structure [154]. These microscopic changes generally precede macroscopic changes in tumor volume, which oc-



cur at much later stages after therapeutic insult. On the other hand, quantitative sodium MRI can give direct information of the intracellular and extracellular sodium concentrations, which depend on the good function of the sodium channels and  $\text{Na}^+/\text{K}^+$ -ATPase in the cell membrane and cellular energy consumption. Therefore any disruption in cellular integrity can lead to abnormal imbalances that are detectable using sodium MRI.

Schepkin et al. [155] studied the possibility of using DWI and sodium MRI for assessing non-invasively the effect of chemotherapeutic treatment of tumors *in vivo*. The study was performed on 9L gliosarcomas implanted in rats and then treated with varying doses of BCNU. MRI were acquired at 21.1T. Main results are shown in Fig. 3.8.1 A-B. This study demonstrate that there is a very good correlation between DWI and sodium MRI in their ability to reveal the efficacy of tumor therapy in a few days following treatment in a dose dependent manner. As both these methods rely on biophysical properties driven by changes in cellular structure (though slightly different), it was expected that they should provide similar results.

Babsky et al. [152] implanted fibrosarcoma (RIF-1) tumors in mice and monitored the effects of 5-fluorouracil (5FU) treatment with proton DWI, SQ and TQF sodium MRI and also PET for measuring Fluorodeoxyglucose (FDG) uptake in the tumor. Tumor volumes significantly decreased in treated animals and slightly increased in control tumors ones 2 and 3 days post-treatment. SQ sodium signal intensity (SI) and water ADC increased in treated tumors but not in control tumors during the same period. TQF sodium SI and FDG uptake were significantly lower in treated tumors compared with control tumors 3 days after 5FU treatment. They concluded that the correlated increases in SQ sodium SI and water ADC following chemotherapy might reflect an increase in extracellular space, while the lower TQF sodium signal and FDG uptake in treated tumors compared with control tumors suggest a shift in tumor metabolism from glycolysis to oxidation and/or a decrease in cell density. A multiparametric approach using  $^1\text{H}+^{23}\text{Na}$  MRI, PET and histology could therefore provide a clearer understanding of the relationship between metabolic and ionic changes in tumors caused by chemotherapies.

Kline et al. [40] used sodium MRI with IR to monitor the response to chemotherapy of mouse xenograft tumors propagated from human prostate cancer cell lines, in order to increase the weighting of the images toward intracellular sodium content. A 37% increase in sodium signal intensity was observed between images before and 24h after administration of antineoplastics, which may due to an increase of intracellular sodium in the treated tumors due. These findings can be matched with experiments with these same drugs and cells treated in culture, where a significant intracellular sodium elevation (10-20 mM) was detected using a ratiometric fluorescent dye. Flow cytometry also showed that this intracellular sodium increase preceded cell death by apoptosis. Sodium MRI with IR seems to increase the weight of the images to intracellular sodium and could help monitoring non-invasively apoptosis of tumors cells induced by chemotherapy.

## Tumor and Chemotherapeutic Response

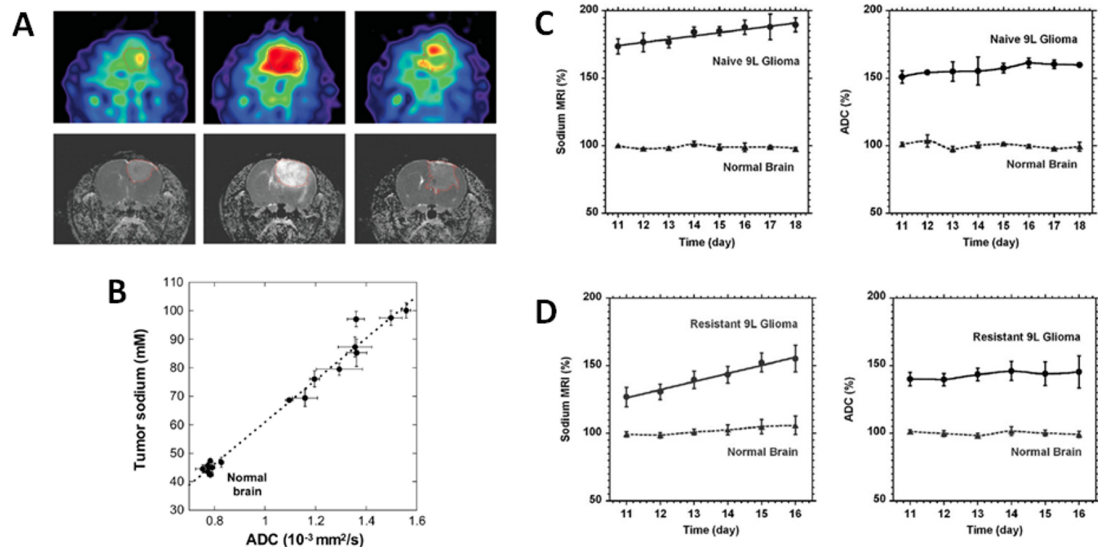


**Figure 3.8.1:** Examples of sodium MRI and proton DWI studies on tumor and chemotherapeutic response in a rat glioma. **A.** Sodium images (top) and proton ADC maps (bottom) of a BCNU-treated 9L rat glioma acquired at day 0, 7 and 23 (left to right) after BCNU injection, performed at day 17 after tumor implantation. Central sodium image at day 7 show a dramatic increase of sodium concentration throughout the entire tumor area. Image at day 23 shows tumor regrowth after tumor shrinking started at day 9 and its maximum regression at day 16. **B.** Correlation of tumor sodium concentration and ADC in the rat glioma obtained at various points following a single dose of BCNU. **C.** Time course after tumor implantation of sodium (left) and ADC (right) variations for a naive type 9L glioma. Sodium and ADC data are given in percent relative to normal contralateral brain. All data are presented as mean  $\pm$  standard deviation. Sodium concentration steadily increased in the naive tumor with a rate of 2.4% per day while ADC was practically unchanged (1.4% per day). **D.** Time course after tumor implantation of sodium (left) and ADC (right) variations for a glioma created from a resistant 9L cell line. Sodium concentration steadily increased in the resistant tumor with a rate of 5.8 % per day while ADC was practically unchanged (1.2% per day). Sodium values were corrected for partial volume effect. Figures A and B from Schepkin V.D et al. *Magnetic Resonance in Medicine* 53:85 92, 2005. Figures C and D from Schepkin V.D. et al. *Magnetic Resonance in Medicine* 67:1159 1166, 2012. Reproduced by permission of Wiley-Blackwell.

### Tumor Resistance to Therapy

Schepkin et al. [156] also studied the capability of sodium MRI and DWI for monitoring the tumor resistance to chemotherapy in intracranial rat 9L gliomas, in order to see if these methods could be used as biomarkers for drug resistance. It was first measured that implanted resistant 9L cells created tumors with significantly reduced TSC (57 mM) than nonresistant (naive) 9L cells (78 mM) and that corresponding differences in ADC were less pronounced but still statistically significant.

The main results are presented in Fig. 3.8.1 C-D which shows the time course evolution of sodium content and ADC in naive and resistant tumors after chemotherapeutic injection (BCNU).



### *3.8 Cancer and Chemotherapeutic Response*

Both Sodium and ADC can differentiate resistant from naive tumors. It is shown that sodium content and ADC vary at very different rates in the two kinds of tumors after treatment and thus must depend on different mechanisms. Many parameters are involved such as tumor volume change, increased extracellular volume, increased intracellular sodium concentration due to deficit in ATP production, increase of blood supply, lactate overproduction (indicator of increased glycolysis). As lactate production tends to correlate with tumor aggressiveness, the increasing intracellular sodium content could be an indicator of growing tumor malignancy. No definite answer can be given but it seems that an increase in intracellular sodium might be the main mechanism involved in the detected increase of sodium signal.

This study shows that TSC measured with sodium MRI could give important information about the level of drug resistance before chemotherapy and that it is more sensitive than DWI for detecting small changes in tumor resistance.



## Conclusion

We have seen that sodium MRI can help assess directly, in a non-invasive and quantitative manner, some important new metabolic information such as tissue viability, through cell integrity and energy status, and that this information cannot be determined by standard anatomical or functional proton MRI or other non-invasive imaging modality.

From the research point of view, there is an increasing interest in this technique, as more and more tissues and diseases are investigated, from brain tumors or strokes to osteoarthritis in articular cartilage, passing through kidney impairments and diabetes in muscles. However, more research still needs to be on both software and hardware for improving the data acquisitions and reconstructions, and increasing the sensitivity of the technique to specific sodium parameters (e.g. intracellular sodium or relaxation times).

From the medical point of view, more research still has to be performed *in vivo*, on more patients with diseases (longitudinal studies) or healthy subjects (optimization of data acquisitions and reconstruction) in order to convince radiologist/physicians that sodium MRI could add some crucial information for the diagnosis but also prognosis of diseases, for the management of patients (e.g. with stroke) or about the possible outcomes of treatments (chemotherapy resistance).

And last but not least, from the commercial point of view, sodium MRI cannot become a clinical tool without the help of the major scanner vendors which should help develop multichannel-multinuclear hardware, new multi-tuned RF coils and new UTE sequences and reconstruction algorithms along with the availability of high magnetic fields (>3T).



## Bibliography

- [1] M. Burnier. *Sodium in health and disease*. Informa Healthcare USA, Inc, New York, 2008.
- [2] E. Murphy and D. A. Eisner. Regulation of intracellular and mitochondrial sodium in health and disease. *Circ Res*, 104(3):292–303, 2009.
- [3] A. M. Rose and R. Valdes. Understanding the Sodium-Pump and Its Relevance to Disease. *Clin Chem*, 40(9):1674–1685, 1994.
- [4] J. C. Skou and M. Esmann. The Na,K-ATPase. *J Bioenergetics Biomembranes*, 24(3):249–261, 1992.
- [5] F. Bloch, WW Hansen, and M. Packard. Nuclear induction. *Phys Rev*, 70(7-8):460–474, 1946.
- [6] E. M. Purcell, H. C. Torrey, and R. V. Pound. Resonance Absorption by Nuclear Magnetic Moments in a Solid. *Phys Rev*, 69(1-2):37–38, 1946.
- [7] H. J. Berendsen and H. T. Edzes. The observation and general interpretation of sodium magnetic resonance in biological material. *Ann NY Acad Sci*, 204:459–85, 1973.
- [8] J. A. Magnuson and N. S. Magnuson. NMR studies of sodium and potassium in various biological tissues. *Ann NY Acad Sci*, 204:297–309, 1973.
- [9] D. A. Feinberg, L. A. Crooks, L. Kaufman, M. Brant Zawadzki, J. P. Posin, M. Arakawa, J. C. Watts, and J. Hoenninger. Magnetic-Resonance Imaging Performance - a Comparison of Sodium and Hydrogen. *Radiology*, 156(1):133–138, 1985.
- [10] A. A. Maudsley and S. K. Hilal. Biological Aspects of Na-23 Imaging. *British Med Bull*, 40(2):165–166, 1984.
- [11] M. E. Moseley, W. M. Chew, M. C. Nishimura, T. L. Richards, J. Murphy-Boesch, G. B. Young, T. M. Marschner, L. H. Pitts, and T. L. James. In vivo sodium-23 magnetic resonance surface coil imaging: observing experimental cerebral ischemia in the rat. *Magn Reson Imaging*, 3(4):383–7, 1985.
- [12] S. K. Hilal, A. A. Maudsley, J. B. Ra, H. E. Simon, P. Roschmann, S. Wittekoek, Z. H. Cho, and S. K. Mun. In vivo NMR imaging of sodium-23 in the human head. *J Comput Assist Tomogr*, 9(1):1–7, 1985.
- [13] J. B. Ra, S. K. Hilal, C. H. Oh, and I. K. Mun. In vivo magnetic resonance imaging of sodium in the human body. *Magn Reson Med*, 7(1):11–22, 1988.

## Bibliography

- [14] W. Grodd and U. Klose. Sodium-MR-Imaging of the Brain - Initial Clinical-Results. *Neuroradiology*, 30(5):399–407, 1988.
- [15] F. E. Boada, J. S. Gillen, G. X. Shen, S. Y. Chang, and K. R. Thulborn. Fast three dimensional sodium imaging. *Magn Reson Med*, 37(5):706–15, 1997.
- [16] S. Wimperis and B. Wood. Triple-Quantum Sodium Imaging. *J Magn Reson*, 95(2):428–436, 1991.
- [17] A. Borthakur, I. Hancu, F. E. Boada, G. X. Shen, E. M. Shapiro, and R. Reddy. In vivo triple quantum filtered twisted projection sodium MRI of human articular cartilage. *J Magn Reson*, 141(2):286–90, 1999.
- [18] I. Hancu, F. E. Boada, and G. X. Shen. Three-dimensional triple-quantum-filtered  $^{23}\text{Na}$  imaging of in vivo human brain. *Magn Reson Med*, 42(6):1146–54, 1999.
- [19] G. Jaccard, S. Wimperis, and G. Bodenhausen. Multiple Quantum NMR-Spectroscopy of  $S=3/2$  Spins in Isotropic Phase: a New Probe for Multiexponential Relaxation. *J Chem Phys*, 85(11):6282–6293, 1986.
- [20] G. J. Bowden and W. D. Hutchison. Tensor Operator-Formalism for Multiple-Quantum NMR. 1. Spin-1 Nuclei, journal = J Magn Reson. 67(3):403–414, 1986.
- [21] G. J. Bowden, W. D. Hutchison, and J. Khachan. Tensor Operator-Formalism for Multiple-Quantum NMR. 2. Spins-3/2, Spin-2, and Spin-5/2 and General-I. *J Magn Reson*, 67(3):415–437, 1986.
- [22] J. R. C. Van der Maarel. Thermal relaxation and coherence dynamics of spin 3/2. I. Static and fluctuating quadrupolar interactions in the multipole basis. *Concepts in Magnetic Resonance Part A*, 19A(2):97–116, 2003.
- [23] A. Jerschow. From Nuclear Structure to the Quadrupolar NMR Interaction and High-Resolution Spectroscopy. *Prog NMR Spec*, 46:63–78, 2005.
- [24] W. D. Rooney and C. S. Springer. A Comprehensive Approach to the Analysis and Interpretation of the Resonances of Spins 3/2 from Living Systems. *NMR Biomed*, 4(5):209–226, 1991.
- [25] R. Kemp-Harper, S. P. Brown, C. E. Hughes, P. Styles, and S. Wimperis. Na-23 NMR methods for selective observation of sodium ions in ordered environments. *Prog NMR Spec*, 31:287–287, 1997.
- [26] W. D. Rooney and C. S. Springer. The Molecular Environment of Intracellular Sodium - Na-23 NMR Relaxation. *NMR Biomed*, 4(5):227–245, 1991.
- [27] A. Borthakur, E. Mellon, S. Niyogi, W. Witschey, J. B. Kneeland, and R. Reddy.
- [28] C.S. Springer. Biological Systems: Spin-3/2 Nuclei. *Encyclopedia of Magnetic Resonance*, 2007.
- [29] G. Navon, H. Shinar, U. Eliav, and Y. Seo. Multiquantum filters and order in tissues. *NMR Biomed*, 14(2):112–132, 2001.
- [30] C. W. Chung and S. Wimperis. Optimum Detection of Spin-3/2 Biexponential Relaxation Using Multiple-Quantum Filtration Techniques. *J Magn Reson*, 88(2):440–447, 1990.

- [31] G. Bodenhausen. Multiple-Quantum NMR. *Prog NMR Spec*, 14:137–173, 1980.
- [32] R. Reddy, M. Shinnar, Z. Wang, and J. S. Leigh. Multiple-Quantum Filters of Spin-3/2 with Pulses of Arbitrary Flip Angle. *J Magn Reson Series B*, 104(2):148–152, 1994.
- [33] R. B. Hutchison and J. I. Shapiro. Measurement of intracellular sodium with NMR methods. *Concepts Magn Reson*, 3:215–263, 1991.
- [34] R. K. Gupta, P. Gupta, and R. D. Moore. Nmr-Studies of Intracellular Metal-Ions in Intact-Cells and Tissues. *Annual Review of Biophysics and Bioengineering*, 13:221–246, 1984.
- [35] H. Naritomi, M. Kanashiro, M. Sasaki, Y. Kuribayashi, and T. Sawada. In vivo Measurements of Intracellular and Extracellular Na<sup>+</sup> and Water in the Brain and Muscle by Nuclear-Magnetic-Resonance Spectroscopy with Shift-Reagent. *Biophys J*, 52(4):611–616, 1987.
- [36] P. M. Winter and N. Bansal. TmDOTP5- as a Na-23 shift reagent for the subcutaneously implanted 9L gliosarcoma in rats. *Magn Reson Med*, 45(3):436–442, 2001.
- [37] J. W. van der Veen, P. van Gelderen, J. H. Creyghton, and W. M. Bovee. Diffusion in red blood cell suspensions: separation of the intracellular and extracellular NMR sodium signal. *Magn Reson Med*, 29(4):571–4, 1993.
- [38] R. Stobbe and C. Beaulieu. In vivo sodium magnetic resonance imaging of the human brain using soft inversion recovery fluid attenuation. *Magn Reson Med*, 54(5):1305–10, 2005.
- [39] G. Madelin, J. S. Lee, S. Inati, A. Jerschow, and R. R. Regatte. Sodium inversion recovery MRI of the knee joint in vivo at 7T. *J Magn Reson*, 207(1):42–52, 2010.
- [40] R. P. Kline, E. X. Wu, D. P. Petrylak, M. Szabolcs, P. O. Alderson, M. L. Weisfeldt, P. Cannon, and J. Katz. Rapid in vivo monitoring of chemotherapeutic response using weighted sodium magnetic resonance imaging. *Clin Cancer Res*, 6(6):2146–56, 2000.
- [41] G. Navon. Complete elimination of the extracellular <sup>23</sup>Na NMR signal in triple quantum filtered spectra of rat hearts in the presence of shift reagents. *Magn Reson Med*, 30(4):503–6, 1993.
- [42] U. Eliav, H. Shinar, and G. Navon. The Formation of a 2nd-Rank Tensor in Na-23 Double-Quantum-Filtered NMR as an Indicator for Order in a Biological Tissue. *J Magn Reson*, 98(1):223–229, 1992.
- [43] J. Pekar and J. S. Leigh. Detection of Biexponential Relaxation in Na-23 Facilitated by Double-Quantum Filtering. *J Magn Reson*, 69(3):582–584, 1986.
- [44] J. Pekar, P. F. Renshaw, and J. S. Leigh. Selective Detection of Intracellular Sodium by Coherence-Transfer NMR. *J Magn Reson*, 72(1):159–161, 1987.
- [45] L. A. Jelicks and R. K. Gupta. On the extracellular contribution to multiple quantum filtered <sup>23</sup>Na NMR of perfused rat heart. *Magn Reson Med*, 29(1):130–3, 1993.
- [46] L. A. Jelicks and R. K. Gupta. Double-Quantum NMR of Sodium-Ions in Cells and Tissues - Paramagnetic Quenching of Extracellular Coherence. *J Magn Reson*, 81(3):586–592, 1989.

## Bibliography

- [47] T. B. Parrish, D. S. Fieno, S. W. Fitzgerald, and R. M. Judd. Theoretical basis for sodium and potassium MRI of the human heart at 1.5 T. *Magn Reson Med*, 38(4):653–61, 1997.
- [48] S. Nielles-Vallespin, M. A. Weber, M. Bock, A. Bongers, P. Speier, S. E. Combs, J. Wohrle, F. Lehmann-Horn, M. Essig, and L. R. Schad. 3D radial projection technique with ultrashort echo times for sodium MRI: clinical applications in human brain and skeletal muscle. *Magn Reson Med*, 57(1):74–81, 2007.
- [49] A. M. Nagel, F. B. Laun, M. A. Weber, C. Matthies, W. Semmler, and L. R. Schad. Sodium MRI using a density-adapted 3D radial acquisition technique. *Magn Reson Med*, 62(6):1565–73, 2009.
- [50] F. E. Boada, G. X. Shen, S. Y. Chang, and K. R. Thulborn. Spectrally weighted twisted projection imaging: reducing T2 signal attenuation effects in fast three-dimensional sodium imaging. *Magn Reson Med*, 38(6):1022–8, 1997.
- [51] A. M. Lu, I. C. Atkinson, T. C. Claiborne, F. C. Damen, and K. R. Thulborn. Quantitative Sodium Imaging With a Flexible Twisted Projection Pulse Sequence. *Magn Reson Med*, 63(6):1583–1593, 2010.
- [52] P. T. Gurney, B. A. Hargreaves, and D. G. Nishimura. Design and analysis of a practical 3D cones trajectory. *Magn Reson Med*, 55(3):575–82, 2006.
- [53] J.G. Pipe, N.R. Zwart, E.A. Aboussouan, R.K. Robison, A. Devaraj, and K.O. Johnson. A new design and rationale for 3D orthogonally oversampled k-space trajectories. *Magn Reson Med*, 66(5):1303–1311, 2011.
- [54] S. Romanzetti, M. Halse, J. Kaffanke, K. Zilles, B. J. Balcom, and N. J. Shah. A comparison of three SPRITE techniques for the quantitative 3D imaging of the Na-23 spin density on a 4T whole-body machine. *J Magn Reson*, 179(1):64–72, 2006.
- [55] B. J. Balcom, R. P. MacGregor, S. D. Beyea, D. P. Green, R. L. Armstrong, and T. W. Bremner. Single-point ramped imaging with T-1 enhancement (SPRITE). *J Magn Reson A*, 123(1):131–134, 1996.
- [56] D. Idiyatullin, C. Corum, J. Y. Park, and M. Garwood. Fast and quiet MRI using a swept radiofrequency. *J Magn Reson*, 181(2):342–349, 2006.
- [57] M. Weiger, K. P. Pruessmann, and F. Hennel. MRI with Zero Echo Time: Hard versus Sweep Pulse Excitation. *Magn Reson Med*, 66(2):379–389, 2011.
- [58] D. M. Grodzki, P. M. Jakob, and B. Heismann. Ultrashort echo time imaging using pointwise encoding time reduction with radial acquisition (PETRA). *Magn Reson Med*, 67(2):510–518, 2012.
- [59] J. D. Osullivan. A Fast Sinc Function Gridding Algorithm for Fourier Inversion in Computer-Tomography. *IEEE Trans Med Imaging*, 4(4):200–207, 1985.
- [60] H. Sedarat and D. G. Nishimura. On the optimality of the gridding reconstruction algorithm. *IEEE Trans Med Imaging*, 19(4):306–17, 2000.



- [61] H. Schomberg and J. Timmer. The gridding method for image reconstruction by Fourier transformation. *IEEE Trans Med Imaging*, 14(3):596–607, 1995.
- [62] J. A. Fessler. On NUFFT-based gridding for non-Cartesian MRI. *J Magn Reson*, 188(2):191–5, 2007.
- [63] L. Greengard and J.Y. Lee. Accelerating the nonuniform fast Fourier transform. *SIAM Review*, 46(3):443–454, 2004.
- [64] T. Knopp, S. Kunis, and D. Potts. A note on the iterative MRI reconstruction from nonuniform k-space data. *Int J Biomed Imaging*, 24727:1–9, 2007.
- [65] K.T. Block, M. Uecker, and J. Frahm. Undersampled radial MRI with multiple coils. Iterative image reconstruction using a total variation constraint. *Magn Reson Med*, 57(6):1086–1098, 2007.
- [66] L. Ying and Z. P. Liang. Parallel MRI Using Phased Array Coils. *IEEE Sign Process*, 27(4):90–98, 2010.
- [67] M. Lustig, D. Donoho, and J. M. Pauly. Sparse MRI: The application of compressed sensing for rapid MR imaging. *Magn Reson Med*, 58(6):1182–1195, 2007.
- [68] L. Fleysher, N. Oesingmann, and M. Inglese. B<sub>0</sub> inhomogeneity-insensitive triple-quantum-filtered sodium imaging using a 12-step phase-cycling scheme. *NMR Biomed*, 23(10):1191–8, 2010.
- [69] J. S. Lee, R. R. Regatte, and A. Jerschow. Optimal control NMR differentiation between fast and slow sodium. *Chem Phys Lett*, 494(4-6):331–336, 2010.
- [70] J. S. Lee, R. R. Regatte, and A. Jerschow. Optimal excitation of Na-23 nuclear spins in the presence of residual quadrupolar coupling and quadrupolar relaxation. *J Chem Phys*, 131(17), 2009.
- [71] F. E. Boada, G. LaVerde, C. Jungreis, E. Nemoto, C. Tanase, and I. Hancu. Loss of cell ion homeostasis and cell viability in the brain: what sodium MRI can tell us. *Curr Top Dev Biol*, 70:77–101, 2005.
- [72] R. Ouwerkerk. Sodium MRI. *Methods Mol Biol*, 711:175–201, 2011.
- [73] T. Hashimoto, H. Ikehira, H. Fukuda, A. Yamaura, O. Watanabe, Y. Tateno, R. Tanaka, and H. E. Simon. In vivo sodium-23 MRI in brain tumors: evaluation of preliminary clinical experience. *Am J Physiol Imaging*, 6(2):74–80, 1991.
- [74] S. S. Winkler. Na-23 Magnetic-Resonance Brain Imaging. *Neuroradiology*, 32(5):416–420, 1990.
- [75] D. P. Fiege, S. Romanzetti, C. C. Mirkes, D. Brenner, and N. J. Shah. Simultaneous single-quantum and triple-quantum-filtered MRI of <sup>23</sup>Na (SISTINA). *Magn Reson Med*, 2012.
- [76] A. Tsang, R. W. Stobbe, and C. Beaulieu. Triple-quantum-filtered sodium imaging of the human brain at 4.7T. *Magn Reson Med*, 67(6):1633–43, 2012.
- [77] A. M. Nagel, M. Bock, C. Hartmann, L. Gerigk, J. O. Neumann, M. A. Weber, M. Bendszus, A. Radbruch, W. Wick, H. P. Schlemmer, W. Semmler, and A. Biller. The potential of relaxation-weighted sodium magnetic resonance imaging as demonstrated on brain tumors. *Invest Radiol*, 46(9):539–47, 2011.

## Bibliography

- [78] K. R. Thulborn, A. M. Lu, I. C. Atkinson, F. Damen, and J. L. Villano. Quantitative Sodium MR Imaging and Sodium Bioscales for the Management of Brain Tumors. *Neuroimag Clin N Am*, 19(4):615–624, 2009.
- [79] L. Fleysheer, N. Oesingmann, R. Brown, D. K. Sodickson, G. C. Wiggins, and M. Inglese. Noninvasive quantification of intracellular sodium in human brain using ultrahigh-field MRI. *NMR Biomed*, 2012.
- [80] The National Institute of Neurological Disorders and Stroke rt PA Stroke Study Group. Tissue plasminogen activator for acute ischemic stroke. *N Engl J Med*, 333(24):1581–1587, 1995.
- [81] R. Luybaert, S. Boujraf, S. Sourbron, and M. Osteaux. Diffusion and perfusion MRI: basic physics. *Eur J Radiol*, 38(1):19–27, 2001.
- [82] G. Schlaug, A. Benfield, A. E. Baird, B. Siewert, K. O. Lovblad, R. A. Parker, R. R. Edelman, and S. Warach. The ischemic penumbra: operationally defined by diffusion and perfusion MRI. *Neurology*, 53(7):1528–37, 1999.
- [83] T. Neumann-Haefelin, H. J. Wittsack, F. Wenserski, M. Siebler, R. J. Seitz, U. Modder, and H. J. Freund. Diffusion- and perfusion-weighted MRI. The DWI/PWI mismatch region in acute stroke. *Stroke*, 30(8):1591–7, 1999.
- [84] T. Ueda, W. T. Yuh, and T. Taoka. Clinical application of perfusion and diffusion MR imaging in acute ischemic stroke. *J Magn Reson Imaging*, 10(3):305–9, 1999.
- [85] A. Tsang, R. W. Stobbe, N. Asdaghi, M. S. Hussain, Y. A. Bhagat, C. Beaulieu, D. Emery, and K. S. Butcher. Relationship between sodium intensity and perfusion deficits in acute ischemic stroke. *J Magn Reson Imaging*, 33(1):41–7, 2011.
- [86] F. E. Boada, Y. X. Qian, E. Nemoto, T. Jovin, C. Jungreis, S. C. Jones, J. Weimer, and V. Lee. Sodium MRI and the Assessment of Irreversible Tissue Damage During Hyper-Acute Stroke. *Translational Stroke Research*, 3(2):236–245, 2012.
- [87] M. S. Hussain, R. W. Stobbe, Y. A. Bhagat, D. Emery, K. S. Butcher, D. Manawadu, N. Rizvi, P. Maheshwari, J. Scozzafava, A. Shuaib, and C. Beaulieu. Sodium imaging intensity increases with time after human ischemic stroke. *Ann Neurol*, 66(1):55–62, 2009.
- [88] K. R. Thulborn, T. S. Gindin, D. Davis, and P. Erb. Comprehensive MR imaging protocol for stroke management: Tissue sodium concentration as a measure of tissue viability in nonhuman primate studies and in clinical studies. *Radiology*, 213(1):156–166, 1999.
- [89] K. R. Thulborn, D. Davis, J. Snyder, H. Yonas, and A. Kassam. Sodium MR imaging of acute and subacute stroke for assessment of tissue viability. *Neuroimag Clin N Am*, 15(3):639–653, 2005.
- [90] D. Hanahan and R.A. Weinberg. The hallmarks of cancer. *cell*, 100(1):57–70, 2000.
- [91] D. Rotin, D. Steelenorwood, S. Grinstein, and I. Tannock. Requirement of the Na<sup>+</sup>/H<sup>+</sup> Exchanger for Tumor-Growth. *Cancer Res*, 49(1):205–211, 1989.
- [92] M. Spector, S. O’Neal, and E. Racker. Reconstitution of the Na<sup>+</sup>K<sup>+</sup> pump of Ehrlich ascites tumor and enhancement of efficiency by quercetin. *J Biol Chem*, 255(12):5504–7, 1980.

- [93] I. L. Cameron, N. K. R. Smith, T. B. Pool, and R. L. Sparks. Intracellular Concentration of Sodium and Other Elements as Related to Mitogenesis and Oncogenesis In vivo. *Cancer Res*, 40(5):1493–1500, 1980.
- [94] R. Ouwerkerk, K. B. Bleich, J. S. Gillen, M. G. Pomper, and P. A. Bottomley. Tissue sodium concentration in human brain tumors as measured with <sup>23</sup>Na MR imaging. *Radiology*, 227(2):529–37, 2003.
- [95] N. Weidner. Tumor angiogenesis: review of current applications in tumor prognostication. *Semin Diagn Pathol*, 10(4):302–13, 1993.
- [96] C. Bjartmar and B.D. Trapp. Axonal and neuronal degeneration in multiple sclerosis: mechanisms and functional consequences. *Curr Opin Neurol*, 14(3):271–278, 2001.
- [97] S. G. Waxman. Mechanisms of Disease: sodium channels and neuroprotection in multiple sclerosis - current status. *Nature Clinic Pract Neurol*, 4(3):159–169, 2008.
- [98] S. G. Waxman, M. J. Craner, and J. A. Black. Na<sup>+</sup> channel expression along axons in multiple sclerosis and its models. *Trends Pharmacolog Sci*, 25(11):584–591, 2004.
- [99] M. Inglese, G. Madelin, N. Oesingmann, JS Babb, W. Wu, B. Stoeckel, J. Herbert, and G. Johnson. Brain tissue sodium concentration in multiple sclerosis: a sodium imaging study at 3 tesla. *Brain*, 133(3):847–857, 2010.
- [100] W. Zaaraoui, S. Konstandin, B. Audoin, A. M. Nagel, A. Rico, I. Malikova, E. Soulier, P. Viout, S. Confort-Gouny, P. J. Cozzone, J. Pelletier, L. R. Schad, and J. P. Ranjeva. Distribution of Brain Sodium Accumulation Correlates with Disability in Multiple Sclerosis: A Cross-sectional <sup>23</sup>Na MR Imaging Study. *Radiology*, 264(3):859–867, 2012.
- [101] E. A. Mellon, D. T. Pilkinton, C. M. Clark, M. A. Elliott, 2nd Witschey, W. R., A. Borthakur, and R. Reddy. Sodium MR imaging detection of mild Alzheimer disease: preliminary study. *Am J Neuroradiol*, 30(5):978–84, 2009.
- [102] K. Reetz, S. Romanzetti, I. Dogan, C. Sass, C. J. Werner, J. Schiefer, J. B. Schulz, and N. J. Shah. Increased brain tissue sodium concentration in Huntington's Disease - A sodium imaging study at 4T. *Neuroimage*, 63(1):517–24, 2012.
- [103] P. C. Gotzsche and M. Nielsen. Screening for breast cancer with mammography. *Cochrane Database of Systematic Reviews*, (4), 2009.
- [104] W.A. Berg, J.D. Blume, J.B. Cormack, E.B. Mendelson, D. Lehrer, M. Böhm-Vélez, E.D. Pisano, R.A. Jong, W.P. Evans, M.J. Morton, et al. Combined screening with ultrasound and mammography vs mammography alone in women at elevated risk of breast cancer. *JAMA*, 299(18):2151–2163, 2008.
- [105] E. Warner, H. Messersmith, P. Causer, A. Eisen, R. Shumak, and D. Plewes. Systematic review: Using magnetic resonance imaging to screen women at high risk for breast cancer. *Annals Intern Med*, 148(9):671–679, 2008.

## Bibliography

- [106] R. Ouwerkerk, M. A. Jacobs, K. J. Macura, A. C. Wolff, V. Stearns, S. D. Mezban, N. F. Khouri, D. A. Bluemke, and P. A. Bottomley. Elevated tissue sodium concentration in malignant breast lesions detected with non-invasive  $^{23}\text{Na}$  MRI. *Breast Cancer Res Treat*, 106(2):151–60, 2007.
- [107] M. A. Jacobs, V. Stearns, A. C. Wolff, K. Macura, P. Argani, N. Khouri, T. Tsangaris, P. B. Barker, N. E. Davidson, Z. M. Bhujwalla, D. A. Bluemke, and R. Ouwerkerk. Multiparametric Magnetic Resonance Imaging, Spectroscopy and Multinuclear ( $\text{Na-}^{23}$ ) Imaging Monitoring of Preoperative Chemotherapy for Locally Advanced Breast Cancer. *Acad Radiol*, 17(12):1477–1485, 2010.
- [108] M. A. Jacobs, R. Ouwerkerk, A. C. Wolff, E. Gabrielson, H. Warzecha, S. Jeter, D. A. Bluemke, R. Wahl, and V. Stearns. Monitoring of neoadjuvant chemotherapy using multiparametric,  $(^{23}\text{Na})$  sodium MR, and multimodality (PET/CT/MRI) imaging in locally advanced breast cancer. *Breast Cancer Res Treat*, 128(1):119–26, 2011.
- [109] M. A. Jansen, J. G. Van Emous, M. G. Nederhoff, and C. J. Van Echteld. Assessment of myocardial viability by intracellular  $^{23}\text{Na}$  magnetic resonance imaging. *Circulation*, 110(22):3457–64, 2004.
- [110] M. Horn, C. Weidensteiner, H. Scheffer, M. Meininger, M. de Groot, H. Remkes, C. Dienesch, K. Przyklenk, M. von Kienlin, and S. Neubauer. Detection of myocardial viability based on measurement of sodium content: A  $^{23}\text{Na}$ -NMR study. *Magn Reson Med*, 45(5):756–64, 2001.
- [111] R. Jerecic, M. Bock, S. Nilles-Vallespin, C. Wacker, W. Bauer, and L. R. Schad. ECG-gated  $^{23}\text{Na}$ -MRI of the human heart using a 3D-radial projection technique with ultra-short echo times. *MAGMA*, 16(6):297–302, 2004.
- [112] R. Ouwerkerk, R. G. Weiss, and P. A. Bottomley. Measuring human cardiac tissue sodium concentrations using surface coils, adiabatic excitation, and twisted projection imaging with minimal T-2 losses. *J Magn Reson Imaging*, 21(5):546–555, 2005.
- [113] R. Ouwerkerk, P. A. Bottomley, M. Solaiyappan, A. E. Spooner, G. F. Tomaselli, K. C. Wu, and R. G. Weiss. Tissue sodium concentration in myocardial infarction in humans: A quantitative  $\text{Na-}^{23}$  MR imaging study. *Radiology*, 248(1):88–96, 2008.
- [114] T. Pabst, J. Sandstede, M. Beer, W. Kenn, A. Greiser, M. von Kienlin, S. Neubauer, and D. Hahn. Optimization of ECG-triggered 3D  $\text{Na-}^{23}$  MRI of the human heart. *Magn Reson Med*, 45(1):164–166, 2001.
- [115] T. Clausen.  $\text{Na}^{+}\text{-K}^{+}$  pump regulation and skeletal muscle contractility. *Physiol Rev*, 83(4):1269–1324, 2003.
- [116] M. J. McKenna, J. Bangsbo, and J. M. Renaud. Muscle  $\text{K}^{+}$ ,  $\text{Na}^{+}$ , and  $\text{Cl}^{+}$  disturbances and  $\text{Na}^{+}\text{-K}^{+}$  pump inactivation: implications for fatigue. *J Appl Physiol*, 104(1):288–295, 2008.
- [117] N. Bansal, L. Szczepaniak, D. Ternullo, J. L. Fleckenstein, and C. R. Malloy. Effect of exercise on  $\text{Na-}^{23}$  MRI and relaxation characteristics of the human calf muscle. *J Magn Reson Imaging*, 11(5):532–538, 2000.
- [118] G. Chang, L. Wang, M. E. Schweitzer, and R. R. Regatte. 3D  $^{23}\text{Na}$  MRI of human skeletal muscle at 7 Tesla: initial experience. *Eur Radiol*, 20(8):2039–46, 2010.

- [119] G. Sweeney and A. Klip. Mechanisms and consequences of Na<sup>+</sup>,K<sup>+</sup>-pump regulation by insulin and leptin. *Cell Mol Biol*, 47(2):363–72, 2001.
- [120] A. M. Nagel, E. Amarteifio, F. Lehmann-Horn, K. Jurkat-Rott, W. Semmler, L. R. Schad, and M. A. Weber. 3 Tesla sodium inversion recovery magnetic resonance imaging allows for improved visualization of intracellular sodium content changes in muscular channelopathies. *Invest Radiol*, 46(12):759–66, 2011.
- [121] E. Amarteifio, A. M. Nagel, M. A. Weber, K. Jurkat-Rott, and F. Lehmann-Horn. Hyperkalemic periodic paralysis and permanent weakness: 3-T MR imaging depicts intracellular <sup>23</sup>Na overload—Initial results. *Radiology*, 264(1):154–63, 2012.
- [122] Y. Y. Vilin and P. C. Ruben. Slow inactivation in voltage-gated sodium channels: molecular substrates and contributions to channelopathies. *Cell Biochem Biophys*, 35(2):171–90, 2001.
- [123] T. Kushnir, T. Knubovets, Y. Itzchak, U. Eliav, M. Sadeh, L. Rapoport, E. Kott, and G. Navon. In vivo <sup>23</sup>Na NMR studies of myotonic dystrophy. *Magn Reson Med*, 37(2):192–6, 1997.
- [124] C. D. Constantinides, J. S. Gillen, F. E. Boada, M. G. Pomper, and P. A. Bottomley. Human skeletal muscle: sodium MR imaging and quantification-potential applications in exercise and disease. *Radiology*, 216(2):559–68, 2000.
- [125] W. M. Hofmann and G. L. Denardo. Sodium Flux in Myotonic Muscular Dystrophy. *Am J Physiol*, 214(2):330–336, 1968.
- [126] C. Kopp, P. Linz, L. Wachsmuth, A. Dahlmann, T. Horbach, C. Schofl, W. Renz, D. Santoro, T. Nien-dorf, D. N. Muller, M. Neininger, A. Cavallaro, K. U. Eckardt, R. E. Schmieder, F. C. Luft, M. Uder, and J. Titze. <sup>23</sup>Na magnetic resonance imaging of tissue sodium. *Hypertension*, 59(1):167–72, 2012.
- [127] HJ Mankin, VC Mow, JA Buckwalter, JP Iannotti, and A. Ratcliffe. Form and function of articular cartilage. *Orthop Basic Sci*, pages 1–44, 1994.
- [128] R. R. Regatte, S. V. Akella, A. Borthakur, J. B. Kneeland, and R. Reddy. In vivo proton MR three-dimensional T1rho mapping of human articular cartilage: initial experience. *Radiology*, 229(1):269–74, 2003.
- [129] T. J. Mosher and B. J. Dardzinski. Cartilage MRI T2 relaxation time mapping: overview and applications. *Semin Musculoskelet Radiol*, 8(4):355–68, 2004.
- [130] W. Ling, R. R. Regatte, G. Navon, and A. Jerschow. Assessment of glycosaminoglycan concentration in vivo by chemical exchange-dependent saturation transfer (gagCEST). *PNAS*, 105(7):2266–70, 2008.
- [131] A. Bashir, M. L. Gray, and D. Burstein. Gd-DTPA2- as a measure of cartilage degradation. *Magn Reson Med*, 36(5):665–73, 1996.
- [132] L. Filidoro, O. Dietrich, J. Weber, E. Rauch, T. Oerther, M. Wick, M. F. Reiser, and C. Glaser. High-resolution diffusion tensor imaging of human patellar cartilage: feasibility and preliminary findings. *Magn Reson Med*, 53(5):993–8, 2005.

## Bibliography

- [133] L. M. Lesperance, M. L. Gray, and D. Burstein. Determination of fixed charge density in cartilage using nuclear magnetic resonance. *J Orthop Res*, 10(1):1–13, 1992.
- [134] R. Reddy, E. K. Insko, E. A. Noyszewski, R. Dandora, J. B. Kneeland, and J. S. Leigh. Sodium MRI of human articular cartilage in vivo. *Magn Reson Med*, 39(5):697–701, 1998.
- [135] E. M. Shapiro, A. Borthakur, A. Gougoutas, and R. Reddy. <sup>23</sup>Na MRI accurately measures fixed charge density in articular cartilage. *Magn Reson Med*, 47(2):284–91, 2002.
- [136] A. J. Wheaton, A. Borthakur, E. M. Shapiro, R. R. Regatte, S. V. Akella, J. B. Kneeland, and R. Reddy. Proteoglycan loss in human knee cartilage: quantitation with sodium MR imaging—feasibility study. *Radiology*, 231(3):900–5, 2004.
- [137] R. Reddy, E. K. Insko, and J. S. Leigh. Triple quantum sodium imaging of articular cartilage. *Magn Reson Med*, 38(2):279–84, 1997.
- [138] D. Idiyatullin, C. Corum, S. Moeller, and M. Garwood. Gapped pulses for frequency-swept MRI. *J Magn Reson*, 193(2):267–273, 2008.
- [139] G. Madelin, J. S. Babb, D. Xia, G. Chang, A. Jerschow, and R. R. Regatte. Reproducibility and repeatability of quantitative sodium magnetic resonance imaging in vivo in articular cartilage at 3 T and 7 T. *Magn Reson Med*, 2011.
- [140] G. Madelin, A. Jerschow, and R.R. Regatte. Sodium MRI with fluid suppression: will it improve early detection of osteoarthritis? *Imaging Med*, 3(1):1–4, 2011.
- [141] S. Trattnig, G. H. Welsch, V. Juras, P. Szomolanyi, M. E. Mayerhoefer, D. Stelzeneder, T. C. Mamisch, O. Bieri, K. Scheffler, and S. Zbyn. Na-23 MR Imaging at 7 T after Knee Matrix-associated Autologous Chondrocyte Transplantation: Preliminary Results. *Radiology*, 257(1):175–184, 2010.
- [142] G. Chang, G. Madelin, O. H. Sherman, E. J. Strauss, D. Xia, M. P. Recht, A. Jerschow, and R. R. Regatte. Improved assessment of cartilage repair tissue using fluid-suppressed <sup>23</sup>Na inversion recovery MRI at 7 Tesla: preliminary results. *Eur Radiol*, 22(6):1341–9, 2012.
- [143] E. K. Insko, D. B. Clayton, and M. A. Elliott. In vivo sodium MR imaging of the intervertebral disk at 4 T. *Acad Radiol*, 9(7):800–804, 2002.
- [144] C. Y. Wang, E. McArdle, M. Fenty, W. Witschey, M. Elliott, M. Sochor, R. Reddy, and A. Borthakur. Validation of Sodium Magnetic Resonance Imaging of Intervertebral Disc. *Spine*, 35(5):505–510, 2010.
- [145] JR James, C. Lin, H. Stark, BM Dale, and N. Bansal. Optimization and Characterization of Sodium MRI Using 8-channel <sup>23</sup>Na and 2-channel <sup>1</sup>H RX/TX Coil. In *13th International Conference on Biomedical Engineering*, year = 2009, pages = 138–141, organization = Springer.
- [146] N. Maril, Y. Rosen, G. H. Reynolds, A. Ivanishev, L. Ngo, and R. E. Lenkinski. Sodium MRI of the human kidney at 3 Tesla. *Magn Reson Med*, 56(6):1229–34, 2006.
- [147] Y. Rosen and R. E. Lenkinski. Sodium MRI of a human transplanted kidney. *Acad Radiol*, 16(7):886–9, 2009.

- [148] D. Hausmann, S. Konstandin, F. Wetterling, S. Haneder, A.M. Nagel, D.J. Dinter, S.O. Schönberg, F.G. Zöllner, and L.R. Schad. Apparent Diffusion Coefficient and Sodium Concentration Measurements in Human Prostate Tissue via Hydrogen-1 and Sodium-23 Magnetic Resonance Imaging in a Clinical Setting at 3 T. *Investigative Radiology*, 47(12).
- [149] D. Hausmann, S. Konstandin, F. G. Zollner, S. Haneder, F. Wetterling, A. M. Nagel, D. J. Dinter, S. O. Schonber, and L. Schad.
- [150] M. A. Jacobs, R. Ouwerkerk, I. Kamel, P. A. Bottomley, D. A. Bluemke, and H. S. Kim. Proton, diffusion-weighted imaging, and sodium ( $^{23}\text{Na}$ ) MRI of uterine leiomyomata after MR-guided high-intensity focused ultrasound: a preliminary study. *J Magn Reson Imaging*, 29(3):649–56, 2009.
- [151] F. Wetterling, D. M. Corteville, R. Kalayciyan, A. Rennings, S. Konstandin, A. M. Nagel, H. Stark, and L. R. Schad. Whole body sodium MRI at 3T using an asymmetric birdcage resonator and short echo time sequence: first images of a male volunteer. *Phys Med Biol*, 57(14):4555–4567, 2012.
- [152] A. M. Babsky, H. Zhang, S. K. Hekintyar, G. D. Hutchins, and N. Bansal. Monitoring chemotherapeutic response in RIF-1 tumors by single-quantum and triple-quantum-filtered Na-23 MRI, H-1 diffusion-weighted MRI and PET imaging. *Magn Reson Imaging*, 25(7):1015–1023, 2007.
- [153] V. D. Schepkin, B. D. Ross, T. L. Chenevert, A. Rehemtulla, S. Sharma, M. Kumar, and J. Stojanovska. Sodium magnetic resonance imaging of chemotherapeutic response in a rat glioma. *Magn Reson Med*, 53(1):85–92, 2005.
- [154] T. L. Chenevert, C. R. Meyer, B. A. Moffat, A. Rehemtulla, S. K. Mukherji, S. S. Gebarski, D. J. Quint, Robertson P. L., T. S. Lawrence, L. Junck, J. M. Taylor, T. D. Johnson, Q. Dong, K. M. Muraszko, J. A. Brunberg, and B. D. Ross. Diffusion MRI: a new strategy for assessment of cancer therapeutic efficacy. *Mol Imaging*, 1(4):336–43, 2002.
- [155] V. D. Schepkin, K. C. Lee, K. Kuszpit, M. Muthuswami, T. D. Johnson, T. L. Chenevert, A. Rehemtulla, and B. D. Ross. Proton and sodium MRI assessment of emerging tumor chemotherapeutic resistance. *NMR Biomed*, 19(8):1035–42, 2006.
- [156] V. D. Schepkin, F. C. Bejarano, T. Morgan, S. Gower-Winter, Jr. Ozambela, M., and C. W. Levenson. In vivo magnetic resonance imaging of sodium and diffusion in rat glioma at 21.1 T. *Magn Reson Med*, 67(4):1159–66, 2012.